Published for SISSA by Springer

Received: August 8, 2023
Revised: January 12, 2024
Accepted: May 26, 2024
Published: June 21, 2024

Positivity-causality competition: a road to ultimate EFT consistency constraints

Mariana Carrillo González,[a] **Claudia de Rham**,[a] **Sumer Jaitly**,[a] **Victor Pozsgay**[a] **and Anna Tokareva**[a,b,c]

[a]*Theoretical Physics, Blackett Laboratory, Imperial College, London, SW7 2AZ, U.K.*
[b]*School of Fundamental Physics and Mathematical Sciences, Hangzhou Institute for Advanced Study, UCAS, Hangzhou 310024, China*
[c]*International Centre for Theoretical Physics Asia-Pacific, Beijing/Hangzhou, China*

E-mail: m.carrillo-gonzalez@imperial.ac.uk, c.de-rham@imperial.ac.uk, sumer.jaitly14@imperial.ac.uk, v.pozsgay19@imperial.ac.uk, tokareva@ucas.ac.cn

Abstract: Effective field theories (EFT) are strongly constrained by fundamental principles such as unitarity, locality, causality, and Lorentz invariance. In this paper, we consider the EFT of photons (or other U(1) gauge field) and compare different approaches to obtain bounds on its Wilson coefficients. We present an analytic derivation of the implications of unitarity (linear and non-linear positivity bounds) and compare these constraints with the requirement of causal propagation of the photon modes around non-trivial backgrounds generated by external sources. Within this setup, we find that the low energy causality condition can give complementary constraints to our analytic positivity bounds. In other words, simple analytic techniques can give strong constraints on the allowed region of the photon EFT parameters even when the positivity bounds are not numerically optimized.

Keywords: Effective Field Theories, Scattering Amplitudes

ArXiv ePrint: 2307.04784

https://doi.org/10.1007/JHEP06(2024)146

JHEP06(2024)146

Contents

JHEP06(2024)146

1 Introduction

Effective field theories (EFTs) allow us to describe low-energy physics without the knowledge of the fundamental theory in the ultraviolet (UV). These low-energy descriptions can include any interaction that is consistent with the symmetries of the system and thus can lead to a large number of free parameters. From a phenomenological perspective, bounding these parameters from observations without any theoretical guidance could result in an incorrect estimation of their actual value. Thus, it is desirable to understand how physical principles can reduce the freedom in this large parameter space. The assumption that the ultimate fundamental theory obeys the basic principles of quantum field theory and relativity puts constraints on its low-energy effective description. Namely, imposing unitarity, Lorentz invariance, analyticity, and locality of the scattering amplitudes leads to constraints on the couplings of the low-energy EFT [1–3]. One such class of constraints is termed *positivity bounds*, as the simplest of them require strict positivity of linear combinations of EFT coefficients. The study of positivity bounds fits within the broader program of the S-matrix bootstrap, which aims to map the infinite-dimensional space of possible S-matrices of all consistent quantum field theories [4–7]. Techniques for obtaining positivity bounds have been fruitfully explored in the recent years following the revival due to [1], leading to infinite sets of positivity bounds beyond the forward limit [8–11], for massive spinning particles (particularly spin-2) [12–19], including massless gravity [20–32], massive gravity [33–36],[1] and non-linear bounds from crossing symmetry, Cauchy-Schwarz type inequalities and properties of Gegenbauer polynomials [37–41], as well as applications to the SMEFT [42–49].

In this paper, we will analyze in detail the consequences of one of the physical conditions required to derive positivity bounds, namely causality. By imposing causality one reaches the conclusion that scattering amplitudes are analytic in the complex s plane up to physical poles and branch cuts in the real axis [4, 50–54], which is used to derive positivity bounds. Causality is the requirement that no information can be received before it is generated. For a local field theory, this is encoded in the condition that the retarded Green's function does not have support outside the lightcone, which in turn is a consequence of micro-causality, that is, that commutators of local operators vanish outside the lightcone. Here, we assume that the spacetime in which the fields propagate has a chronology defined by a minimally coupled photon moving at the speed of light. Examples, where this is not assumed have been considered in [55–57] and allow for a large time advance. In such settings, an observable time advance does not imply that we can generate a closed timelike curve as is the case in the examples considered in [1], which also assumes the chronology of the spacetime to be given by the photon as in this paper.

Besides the implications of causality for the derivation of positivity bounds, one can also obtain constraints on the Wilson coefficients of an EFT without any assumptions of the UV by only requiring causal propagation at low energies around non-trivial backgrounds generated by external sources [58–69]. One should note that the strict requirement of a subluminal speed of sound is too strong. Modes can propagate superluminally in small regions of spacetime and not lead to any observable violation of causality. Instead of focusing on the

[1] Note however that the recent work [36] relies on the additional assumption of a purely tree-level completion where the branch-cut starts at best at the cutoff. While this assumption may be appropriate for some non-gravitational theories as we shall discuss here, it is not anticipated to be valid in massive gravity.

JHEP06(2024)146

speed of sound, we will consider a cleaner diagnostic by computing the time delay experienced by a propagating mode in the EFT relative to a free mode. The time delay is invariant under field redefinitions since it is directly related to the S-matrix as

$$\Delta T = -i\left\langle \text{in}\left|\hat{S}^\dagger \frac{\partial}{\partial\omega}\hat{S}\right|\text{in}\right\rangle. \tag{1.1}$$

By defining the scattering phase shift from the S-matrix eigenvalues as $\hat{S}|\,\text{in}\rangle = e^{2i\delta}|\,\text{in}\rangle$, we can compute the time delay at fixed impact parameter

$$\Delta T_b = 2\frac{\partial\delta_\ell}{\partial\omega}\bigg|_b\,, \tag{1.2}$$

which corresponds to the time delay computed in the Eikonal approximation [70, 71]. In order to have a well-defined time delay, one requires a separation of scales between the background and the propagating modes. The scales of variation of the background should be much larger than the wavelength of the mode in order to observe a well-defined phase shift and hence time delay. This means that we will be working in the semi-classical regime, in other words, in the WKB regime. We can now diagnose violations of causality by checking whether a theory can give rise to closed-timelike curves, which is equivalent to obtaining a resolvable time-advance [1, 72]. Additionally, this should be computed within the regime of validity of the EFT and the WKB approximation. The concept of resolvability arises from the uncertainty principle which tells us that, if we have a mode with frequency ω, we cannot measure its time delay/advance if it is smaller than the uncertainty $\Delta t \sim \omega^{-1}$. Thus, if a mode experiences a time advance that is resolvable, that is, a time advance larger than the resolution scale of geometric optics,

$$\Delta T < -1/\omega\,, \tag{1.3}$$

then the theory has a mode that violates causality. Note that there is no strict derivation of this bound such as the Wigner bound in [73]. Nevertheless, there is evidence that this bound should hold for relativistic theories as well [69, 72, 74]. The precise number on the r.h.s. of the equation above has not been determined, but it should be an order one number. We will explore below the consequences of having different values of this order one number. By imposing that our theory does not have any such modes, we can bound the value of Wilson coefficients. In this paper, we will analyze such bounds for the case of an EFT of a photon.

In principle, one would expect that the requirement of causal propagation in the infrared leads to weaker constraints than the requirement of a local, unitary, causal, and Lorentz invariant theory all the way to the UV. Nevertheless, the actual constraints obtained from our requirement of causal propagation and the actual constraints obtained by deriving positivity bounds are not guaranteed to encode the full power of these assumptions. As we will see, it is possible that these bounds test both similar and different regions of the parameter space. Thus, in some cases, causality and positivity can lead to similar bounds, while in other cases they can probe different regions of the parameter space and lead to complementary bounds that can be combined to obtain a much stronger constraint on the Wilson coefficients of the EFT.

The main purpose of this paper is to compare the implications arising from the requirement of causal propagation with the constraints from positivity bounds by considering the example

JHEP06(2024)146

of an EFT of photons. The positivity bounds on the EFT coefficients were studied previously in [1, 38, 75–77]. In this paper, we formulate new constraints on the operators up to dimension-12 (we consider 7 independent couplings) in the form of analytic expressions. We develop a new approach based on scattering amplitudes for indefinite polarization states of photons parameterized by four angles. This allows us to make the bounds stronger than those derived from the scattering of given polarization states, as the obtained inequalities must be valid for all possible indefinite polarization states. We formulate a set of linear positivity bounds derived in a way similar to [9],[2] and analytically perform the optimisation of the inequalities. In addition, we formulate the two non-linear bounds constraining dimension-10 operators between dimension-8 and dimension-12 couplings. We also discuss how one-loop corrections to the amplitudes would affect the bounds.

To compare the strength of the causality and positivity requirements, we consider different slices in the 6-dimensional space of couplings. We show that, in some directions of the parameter space, positivity bounds provide stronger constraints while causality conditions do not lead to compact bounds in all directions. The later is due to technical challenged related to the implementation of the WKB approximation, which prevent us from including non-sign definite contributions to the time delay for certain Wilson coefficients. This does not imply that causality requirements cannot lead to compact bounds in these specific directions, but rather that in some situations, our current setup does not lead to a compact bound in all directions. On the other hand, for dimension-10 operators we obtain compact causality bounds which are so far stronger than the analytic positivity bounds formulated in this work. We emphasize that this does not represent a contradiction but simply signals the fact that the ultimate unitarity constraints must be stronger than those which were formulated so far. Thus, the causality conditions can provide a hint for the formulation of better constraints on the EFT parameter space.

The paper is organised as follows. In section 2 we introduce the photon EFT and review the connection between the Lagrangian and scattering amplitudes parametrisations. In section 3 we describe the novel methods of obtaining positivity bounds for the scattering of indefinite polarization states of photons. Section 4 is dedicated to deriving the causality constraints from the absence of a resolvable time advance in photon propagation on top of a spherically-symmetric background generated by an external source. In section 5, we compare positivity and causality bounds in different slices of the parameter space. After that, in section 6 we present the conclusions and discussion on the complementarity of positivity and causality bounds. Throughout the manuscript, we work in four spacetime dimensions, with signature $(-+++)$.

2 Photon effective field theory

2.1 EFT of U(1) gauge field

The most generic EFT of a massless vector field A_μ enjoying a U(1) gauge symmetry can be formulated in the following way. We define the field-strength (or Faraday) tensor $F_{\mu\nu}$

[2] To the best of our knowledge, the bounds of this type were never formulated before for amplitudes without $s-u$ crossing symmetry.

JHEP06(2024)146

and its Hodge dual $\tilde{F}_{\mu\nu}$ in the following way

$$F_{\mu\nu} = \partial_\mu A_\nu - \partial_\nu A_\mu \,, \qquad \tilde{F}_{\mu\nu} = \frac{1}{2}\epsilon_{\mu\nu\rho\sigma}F^{\rho\sigma} \,. \tag{2.1}$$

We make the hypothesis that the U(1)-symmetric Lagrangian only depends on gauge-invariant quantities, i.e.

$$\mathcal{L}_F = \mathcal{L}(F, \tilde{F}, \partial F, \partial\tilde{F}, \dots) \,. \tag{2.2}$$

Note that we will forbid any operator with an odd number of $\tilde{F}$ to avoid any parity breaking. We will assume that our EFT breaks down at a scale Λ and we will consider operators of at most 4 fields and dimension-12. We assume that operators with more than 4 fields are suppressed at the EFT order that we work at, which allows us to compare the causality bounds to positivity bounds. The precise conditions for the validity of the EFT and the truncation of the infinite series of operators at this order are shown in detail in eq. (4.11). After neglecting redundant terms that can be removed through field redefinitions, we write a set of independent operators up to dimension-12 which reads

$$\begin{aligned}
\mathcal{L} = &-\frac{1}{4}F_{\mu\nu}F^{\mu\nu} \\
&+ \frac{c_1}{\Lambda^4}F^{\mu\nu}F_{\mu\nu}F^{\alpha\beta}F_{\alpha\beta} + \frac{c_2}{\Lambda^4}F^{\mu\nu}F^{\alpha\beta}F_{\mu\alpha}F_{\nu\beta} \\
&+ \frac{c_3}{\Lambda^6}F^{\alpha\mu}F^{\nu\beta}\partial_\mu F_{\beta\gamma}\partial_\nu F_\alpha{}^\gamma + \frac{c_4}{\Lambda^6}F^{\alpha\mu}F^{\nu\beta}\partial_\beta F_{\mu\gamma}\partial^\gamma F_{\alpha\nu} + \frac{c_5}{\Lambda^6}F^{\alpha\mu}F^{\nu\beta}\partial_\beta F_{\nu\gamma}\partial^\gamma F_{\alpha\mu} \\
&+ \frac{c_6}{\Lambda^8}F^{\mu\nu}\partial_\mu F_{\nu\rho}\partial^\rho\partial^\alpha F^{\beta\gamma}\partial_\alpha F_{\beta\gamma} + \frac{c_7}{\Lambda^8}F^\mu{}_\gamma\partial_\mu F_{\nu\rho}\partial^\nu F_{\alpha\beta}\partial^\rho\partial^\gamma F^{\alpha\beta} \\
&+ \frac{c_8}{\Lambda^8}F^{\mu\gamma}\partial_\mu F_{\nu\rho}\partial^\rho\partial^\beta F_{\alpha\gamma}\partial^\alpha F^\nu{}_\beta \,.
\end{aligned} \tag{2.3}$$

The 4-point tree-level scattering amplitude arising from this theory can be parametrized as

$$\mathcal{A}_{++++} = \frac{f_2}{\Lambda^4}\left(s^2+t^2+u^2\right) + \frac{f_3}{\Lambda^6}stu + \frac{f_4}{\Lambda^4}\left(s^2+t^2+u^2\right)^2 \,, \tag{2.4a}$$

$$\mathcal{A}_{++--} = \frac{g_2}{\Lambda^4}s^2 + \frac{g_3}{\Lambda^6}s^3 + \frac{g_4}{\Lambda^8}s^4 + \frac{g_4'}{\Lambda^8}s^2tu \,, \tag{2.4b}$$

$$\mathcal{A}_{+++-} = \frac{h_3}{\Lambda^6}stu \,, \tag{2.4c}$$

where all other helicity configurations can be obtained by symmetry considerations (parity, time-reversal, boson exchange, crossing symmetry) and we consider a set up where all particles are incoming. The scattering amplitude parameters above are related to the Wilson coefficients in eq. (2.3) via

$$\begin{aligned}
&f_2 = 2(4c_1+c_2) \,, && g_2 = 2(4c_1+3c_2) && \\
&f_3 = -3(c_3+c_4+c_5) \,, && g_3 = -c_5 \,, && h_3 = -\frac{3}{2}c_3 \,, \\
&f_4 = \frac{1}{4}c_6 \,, && g_4 = \frac{1}{2}(c_6-c_8)+c_7 \,, && g_4' = -\frac{1}{2}(c_7+c_8) \,.
\end{aligned} \tag{2.5}$$

Note that throughout the text we occasionally refer to the amplitude parameters themselves as 'Wilson coefficients'.

JHEP06(2024)146

UV completion	g_2	f_2	f_3	g_3	h_3	f_4	g_4	g_4'
scalar	1	1	3	1	0	$\frac{1}{2}$	1	0
axion	1	-1	-3	1	0	$-\frac{1}{2}$	1	0
scalar QED	1	$\frac{3}{4}$	$\frac{5}{14}$	$\frac{3}{28}$	$\frac{1}{28}$	$\frac{1}{84}$	$\frac{41}{420}$	$-\frac{1}{168}$
spinor QED	1	$-\frac{3}{11}$	$-\frac{10}{77}$	$\frac{4}{77}$	$-\frac{1}{77}$	$-\frac{1}{231}$	$\frac{13}{660}$	$-\frac{5}{462}$
vector QED	1	$\frac{1}{28}$	$\frac{5}{294}$	$-\frac{47}{1764}$	$\frac{1}{588}$	$\frac{1}{1764}$	$\frac{131}{8820}$	$-\frac{23}{1176}$
spin-2 even I*	1	1	0	1	0	$\frac{1}{2}$	1	-6
spin-2 even II	1	0	0	-1	0	0	1	-2
spin-2 odd*	1	-1	0	1	0	$-\frac{1}{2}$	1	-6
min.-coupled spin-2	1	0	0	$-\frac{1}{2}$	0	0	$\frac{1}{2}$	-1

Table 1. Values of the Wilson coefficients for known partial UV completions, where g_2 is normalized to unity. The partial UV completions with a $*$ superscript do not satisfy the causality and positivity bounds. This simply indicates that the non-minimal couplings that they contain are ruled out; see appendix D for more details.

2.2 Partial UV completions

Together with the positivity and causality bounds, we will show explicitly the values for the coefficients of known partial UV completions. We will focus on tree level, partial UV completions given by the interactions of the photon with a scalar and an axion. In some cases, we will also show the values for the partial UV completions involving a graviton that were analyzed in [75–77]. We refer to the spin-2 partial UV completion from [75] as minimally-coupled spin-2. Lastly, we will also analyze some of these bounds that can be compared to one-loop, partial UV completions from QED-like theories. We will consider the standard (spinor) QED [78–81], scalar QED [82, 83], and vector QED [83, 84]. Table 1 shows the coefficients for all these partial UV completions.

The labels even or odd in principle refer to the theories that propagate only in the even or odd sector. These sectors are defined by the transformation of the partial waves under space inversion; even modes transform with a factor $(-1)^\ell$ and odd modes with a factor $(-1)^{\ell+1}$. Nevertheless, some of the theories labeled below as odd or even do not satisfy this property, but we still use this name as is the one used in the original paper that constructed them [77]. The time delay for the even sector of the axion vanishes as it should. Similarly, the time delay for the odd sector vanishes for the scalar partial UV completions. On the other hand, the so-called odd and even spin-2 partial UV completions do not satisfy this feature. See appendix D for more details.

3 Positivity bounds

In this section, we will explore constraints on the Wilson coefficients of the photon EFT that arise from requiring a so-called 'standard' or 'consistent' UV completion [1]. By 'standard'

JHEP06(2024)146

we mean that the UV theory has an S-matrix satisfying certain properties that encapsulate unitarity, causality, locality, and Lorentz invariance:

- *Unitarity*: the S-matrix being unitary follows from the completeness of the asymptotic in/out Hilbert space and implies the conservation of probability in scattering processes. This leads to the optical theorem, which roughly states that,

$$\mathrm{Im}\mathcal{A}_{i\to i}(s,0) = \frac{1}{2}\sum_n |\mathcal{A}_{i\to n}(s)|^2\,, \tag{3.1}$$

  i.e. that the imaginary part of the elastic scattering amplitude from state i to i is related to the absolute values of the amplitudes for all i to n processes, for any intermediate state n. An immediate consequence of this is that the imaginary part of the forward limit elastic amplitude is positive. Since the imaginary part of the amplitude arises from non-analytic structures such as poles and branch cuts, unitarity also informs us of the analytic structure of the amplitude.

  One slightly more technical statement that we utilise is positivity of t-derivatives of the discontinuity (or imaginary part as phrased above) at $t = 0$. This can be derived from properties of the partial wave expansion, e.g. see [9, 13, 27]. Non-analyticity of the amplitude generated by massless loops can undermine this, however for spin-1 loops it is possible to circumvent this with an IR regulating mass.

- *Causality*: the statement of microcausality in the quantum field theory, i.e. that space-like separated operators commute, is connected to the analytic structure of the amplitude [50]. The amplitude is assumed to be analytic in the upper half complex s plane for fixed negative t. The assumption of the Schwarz reflection property extends this to the lower half plane, with the final result that the amplitude is analytic up to the poles and branch cuts required by unitarity.

- *Locality*: we assume that the fixed t amplitude is polynomially bounded in the complex s plane as $|s| \to \infty$. This assumption is implicit in the derivation of scattering amplitudes via the LSZ prescription as it allows one to Fourier transform between position and momentum space correlation functions. This has been linked in quantum field theory with the notion of locality and is required for the existence of a dispersion relation representation [52, 85].

- *Boundedness*: for theories with a mass gap, the Froissart-Martin bound demands that the elastic amplitude grows slower than s^2 as $|s| \to \infty$, allowing for a twice subtracted dispersion relation to be written. Whilst this boundedness is not proven for theories without a mass gap, we will assume that the exact amplitude obeys this property [86–88].

In this section we assume that there are no poles due to the exchange of states with spin ≥ 2 (such as the infamous t-channel pole arising from graviton exchange) and so we can safely assume any poles have been already subtracted, leaving us with the pole-subtracted amplitude, without violating the boundedness properties of the amplitude.

It is worth emphasizing once more that the positivity bounds obtained here are by no means expected to be the most optimal bounds following from the above assumptions and

JHEP06(2024)146

the dispersion relation, and neither is this the point of this work, however they provide a good starting point for comparing with causality bounds. It is also worth pointing out that in order to make the comparaison with causality bounds more visible, our region plots are in contrast with those that have been obtained in the recent literature [22, 75, 76]. The above works mainly give the allowed region for any two Wilson coefficients as a projection which is independent of the values of the other Wilson coefficients, as is natural in the numerical optimization approach to EFT bounds [41]. In our analysis we explicitly fix the values of the other Wilson coefficients in obtaining our bounds, giving a *slice* of the parameter space, as opposed to a projection. As the primary focus of this work is to compare the positivity and causality bounds, the latter of which apply to slices of the parameter space, it is more sensible to examine slices on the positivity bound side.

3.1 Indefinite helicity amplitudes and manifest crossing symmetry

Positivity bounds can be derived for any scattering amplitude that is elastic, meaning that the initial and final states are the same. In these cases, unitarity implies positivity of the discontinuities of the amplitude. Thus, we construct a general in-going state of two photons, $|\text{in}\rangle = \sum_{h_1,h_2} a_{h_1h_2} |h_1, h_2\rangle$ where the helicity labels are summed over the two polarization states, $h_i = \pm$, and study the elastic scattering of this state. Bounds on such indefinite helicity amplitudes have been fruitfully explored in previous literature [15, 16, 26, 27, 33, 89–91].

As the initial state is a sum of helicity eigenstates, the scattering amplitude will decompose into a sum of amplitudes between helicity eigenstates which notably contains amplitudes for processes that are themselves not elastic. The helicity amplitudes for the process with in-state of helicity $|h_1, h_2\rangle$ and out-state of helicity $|-h_3, -h_4\rangle$ are denoted,

$$\textbf{(in-out)} \qquad \mathcal{A}_{h_1h_2\to -h_3-h_4}(s,t,u) \equiv \mathcal{A}_{h_1h_2h_3h_4}(s,t,u) \qquad \textbf{(all in)}\,. \tag{3.2}$$

Generally crossing relations/symmetries between helicity amplitudes are extremely complicated (see for example [13]) however for the massless, bosonic and equal spin scattering we are interested in, the relations are a lot simpler and are given by,

$$\begin{aligned}
\mathcal{A}_{h_1h_2h_3h_4}(s,t,u) &= \mathcal{A}_{h_1h_4h_3h_2}(u,t,s)\,,\\
\mathcal{A}_{h_1h_2h_3h_4}(s,t,u) &= \mathcal{A}_{h_1h_3h_2h_4}(t,s,u)\,,\\
\mathcal{A}_{h_1h_2h_3h_4}(s,t,u) &= \mathcal{A}_{h_1h_2h_4h_3}(s,u,t)\,.
\end{aligned} \tag{3.3}$$

If we denote the elastic scattering of our generic initial state as the s-channel process, with amplitude $\mathcal{A}_s(s,t,u)$, the corresponding crossed u-channel process will have the amplitude $\mathcal{A}_u(s,t,u)$ given by,

$$\mathcal{A}_u(s,t,u) = \mathcal{A}_s(u,t,s) = \sum_{h_i} a_{h_1h_2} a^*_{-h_3-h_4} \mathcal{A}_{h_1h_2h_3h_4}(u,t,s) \tag{3.4}$$

$$= \sum_{h_i} a_{h_1h_2} a^*_{-h_3-h_4} \mathcal{A}_{h_1h_4h_3h_2}(s,t,u)\,. \tag{3.5}$$

Note that the final expression cannot arise as the amplitude for an elastic scattering process and so we cannot use positivity of the u-channel discontinuity or apply positivity bounds in the usual manner. This can be simply remedied by requiring that the coefficients in our

JHEP06(2024)146

general initial state are factorisable (making it a separable state) such that $a_{h_1h_2} = \alpha_{h_1}\beta_{h_2}$ in which case the above expression becomes,

$$\mathcal{A}_u(s,t,u) = \sum_{h_i} \alpha_{h_1}\beta_{h_2}\alpha^*_{-h_3}\beta^*_{-h_4}\mathcal{A}_{h_1h_4h_3h_2}(s,t,u) \tag{3.6}$$

$$= \sum_{h_i} \alpha_{h_1}\beta^*_{-h_2}\alpha^*_{-h_3}\beta_{h_4}\mathcal{A}_{h_1h_2h_3h_4}(s,t,u)\,, \tag{3.7}$$

which identifies the amplitude $\mathcal{A}_u$ as the elastic amplitude for the initial state, $|\text{in}\rangle = \sum \alpha_{h_1}\beta^*_{-h_2}|h_1h_2\rangle$.

By comparing the above two lines we can deduce that the amplitude will obey manifest $s-u$ crossing symmetry if the β_h coefficients satisfy,

$$\beta_h = \beta^*_{-h}e^{i\gamma} \implies \mathcal{A}_s(s,t,u) = \mathcal{A}_u(s,t,u)\,, \qquad \gamma \in \mathbb{R}\,, \tag{3.8}$$

and similarly manifest $s-t$ crossing symmetry if,

$$\beta_h = \alpha^*_{-h}e^{i\psi} \implies \mathcal{A}_s(s,t,u) = \mathcal{A}_t(s,t,u)\,, \qquad \psi \in \mathbb{R}\,. \tag{3.9}$$

If both the above conditions are satisfied the amplitude will be triple crossing symmetric, i.e. unchanged under any permutation of s,t,u and $\mathcal{A}_s = \mathcal{A}_t = \mathcal{A}_u$. A useful parametrisation of the α,β coefficients that guarantees correct normalisation of states is given by (for real values of the angles and phases),

$$\alpha_+ = \cos\theta\,, \quad \alpha_- = \sin\theta\, e^{\mathrm{i}\phi}\,, \quad \beta_+ = \cos\chi\,, \quad \beta_- = \sin\chi\, e^{\mathrm{i}\psi}\,. \tag{3.10}$$

The motivation for imposing manifest crossing symmetries is that different, a priori stronger positivity bounds can be derived for such amplitudes [40, 41]. Imposing the above conditions amounts to restrictions on the angles introduced in eq. (3.10) and leaves one with families of crossing symmetric amplitudes parameterised by the remaining angles. For example, the one-parameter family of manifestly triple crossing symmetric (which we denote by `stu`) amplitudes is,

$$\mathcal{A}_{\texttt{stu}} = \frac{1}{2}(\mathcal{A}_{++--} + \mathcal{A}_{+--+} + \mathcal{A}_{+-+-}) + 2\mathcal{A}_{+---}\cos\phi + \frac{1}{2}\mathcal{A}_{++++}\cos 2\phi\,, \tag{3.11}$$

whereas the indefinite helicity amplitude with no manifest crossing symmetry, denoted `ih`, is given by,

$$\begin{aligned}\mathcal{A}_{\texttt{ih}} = \frac{1}{2}\Big(&\cos(2\theta)(\mathcal{A}_{++--} - \mathcal{A}_{+--+})\cos(2\chi) + \mathcal{A}_{++--} + 4\mathcal{A}_{+---}\sin(\chi)\cos(\chi)\cos(\psi)\\ &+ \mathcal{A}_{+--+} + \sin(2\theta)\sin(2\chi)(\mathcal{A}_{++++}\cos(\psi+\phi)\\ &+ \mathcal{A}_{+-+-}\cos(\phi-\psi)) + 4\mathcal{A}_{+---}\sin(\theta)\cos(\theta)\cos(\phi)\Big)\,.\end{aligned} \tag{3.12}$$

Finally the manifestly $s-u$ symmetric amplitudes, $\mathcal{A}_{\texttt{su}}$ are obtained by evaluating $\mathcal{A}_{\texttt{ih}}$ on any value of θ or χ such that $\cos(2\theta)\cos(2\chi) = 0$.

JHEP06(2024)146

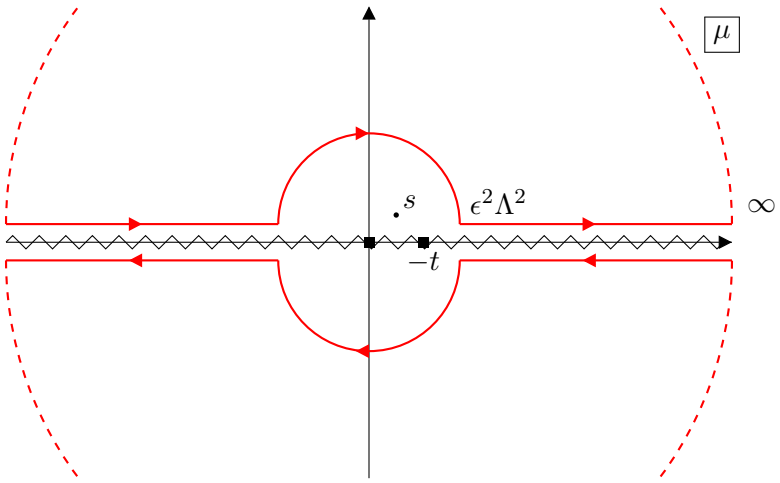

Figure 1. Structure of the pole subtracted amplitude, and the integration contour used for the dispersion relation. The dashed line corresponds to the two arcs at infinity which close the two disjoint contours in the upper and lower half plane. The value of s in the dispersion relation is taken inside the semi-circular region near the origin. The boxes denote the start of the two branch cuts, the s-channel going from $\mu = 0$ to the right and the u-channel from $\mu = -t$ to the left.

3.2 Dispersion relations and positivity bounds

From our assumptions on the UV theory, the analytic structure of the amplitude in the complex s plane for fixed $t < 0$ is known, and depicted in figure 1. Dispersion relations are an essential tool in connecting these UV assumptions to the amplitudes in the EFT; here, we give a brief summary of their derivation. Consider the integral,

$$\frac{1}{2\pi \mathrm{i}}\left(\oint_+ + \oint_-\right)\frac{\mathcal{A}_s(\mu,t)}{(\mu-s)^3}\,\mathrm{d}\mu = 0\,, \tag{3.13}$$

where the two closed contours, labelled $+$ in the upper half plane and $-$ in the lower, are shown in red in figure 1. The branch cuts completely cover the real axis and overlap, so we are forced to use this combination of disjoint contours, rather than the one typically used in situations where there is an analytic region between the cuts. From the residue theorem, we know that both integrals are zero as they contain no poles. Additionally, the assumption that the amplitude grows more slowly than μ^2 as $|\mu| \to \infty$, or in other words that there exists a twice subtracted dispersion relation, implies that the integral over the arcs at infinity vanishes due to the μ^3 suppression in the denominator of the integrand. Separating the remainder of the contour into the path along the branch cuts and the two arcs at the intermediate scale $|\mu| = \epsilon^2\Lambda^2$ one arrives at the dispersion relation,

$$\frac{1}{2\pi \mathrm{i}}\int_{\text{arcs}}\mathrm{d}\mu\,\frac{\mathcal{A}_s(\mu,t)}{(\mu-s)^3} = \int_{\epsilon^2\Lambda^2}^{\infty}\frac{\mathrm{d}\mu}{\pi}\frac{\mathrm{Disc}_s\mathcal{A}_s(\mu,t)}{(\mu-s)^3} + \int_{\epsilon^2\Lambda^2-t}^{\infty}\frac{\mathrm{d}\mu}{\pi}\frac{\mathrm{Disc}_s\mathcal{A}_u(\mu,t)}{(\mu-u)^3}\,, \tag{3.14}$$

where the integral on the left-hand side is taken *anticlockwise* on the arcs at $|\mu| = \epsilon^2\Lambda^2$, i.e. opposite to how is shown in the above figure. The discontinuity is defined as,

$$\mathrm{Disc}_s\mathcal{A}(s,t) \equiv \lim_{\epsilon\to 0^+}\frac{1}{2\mathrm{i}}(\mathcal{A}(s+\mathrm{i}\epsilon,t) - \mathcal{A}(s-\mathrm{i}\epsilon,t))\,, \tag{3.15}$$

JHEP06(2024)146

and under the assumption of the Schwarz reflection principle, $\mathcal{A}(s^*,t)=\mathcal{A}(s,t)^*$, this is equal to the imaginary part of $\mathcal{A}(s,t)$. Note that we have also used crossing symmetry to relate the left-hand branch cut discontinuity of $\mathcal{A}_s$ to the physical right-hand cut of $\mathcal{A}_u$, which also obeys positivity properties as both processes are elastic. Note that the procedure of computing the low energy integral along the arc is equivalent to subtracting the calculable part of the low energy branch cut and subtracting it, i.e. using the *improved positivity bounds*.

The power of the dispersion relation representation comes from the fact that the left-hand side is a low-energy quantity, computable in an effective field theory, whilst the right-hand side includes information about the amplitude at arbitrarily large energy scales in the UV. Therefore it connects the Wilson coefficients of the EFT to a high-energy quantity that can be constrained by our requirements of a consistent UV completion, and thereby, directly constrain the low-energy theory itself. From this point, positivity bounds are a direct consequence of unitarity, which implies positivity of the discontinuities in the integrals of the right-hand side, for all energies. Taking the limit $|s|\to 0$ and $t\to 0^-$ in the dispersion relation gives positive quantities on both sides,

$$\frac{1}{2\pi \mathrm{i}}\int_{\text{arcs}} \mathrm{d}\mu\, \frac{\mathcal{A}_s(\mu,0)}{\mu^3}=\int_{\epsilon^2\Lambda^2}^{\infty}\frac{\mathrm{d}\mu}{\pi}\frac{\text{Disc}_s\mathcal{A}_s(\mu,0)}{\mu^3}+\int_{\epsilon^2\Lambda^2}^{\infty}\frac{\mathrm{d}\mu}{\pi}\frac{\text{Disc}_s\mathcal{A}_u(\mu,0)}{\mu^3}>0\,. \tag{3.16}$$

Inserting the tree-level EFT amplitude $\mathcal{A}_{++--}(s,0)$ into the left-hand side and computing the integral simply yields the coefficient g_2, thus we arrive at the first positivity bound, $g_2>0$.

More generally by taking s and t derivatives of the dispersion relation given by eq. (3.14) and then taking the limits $|s|\to 0$ and $t\to 0^-$ we can derive further positivity statements. There are an infinite number of dispersion relations one could obtain in this way, but as the number of derivatives increases so does the number of Wilson coefficients in the bounds. In order to bound the coefficients g_2, f_2, g_3, f_3, h_3 we shall first examine the leading three dispersion relations. To condense expressions we introduce the notation,

$$C(n,m)\equiv\frac{n!/2}{2\pi\mathrm{i}}\int_{\text{arcs}}\mathrm{d}\mu\,\frac{\partial_t^m\mathcal{A}(\mu,0)}{\mu^{n+1}}\quad\text{and}\quad I_{s,u}(n,m)\equiv\int_{\epsilon^2\Lambda^2}^{\infty}\frac{\mathrm{d}\mu}{\pi}\frac{\partial_t^m\text{Disc}_s\mathcal{A}_{s,u}(\mu,0)}{\mu^{n+1}}>0\,, \tag{3.17}$$

which gives the first three dispersion relations as,

$$\begin{aligned}
C(2,0)&=I_s(2,0)+I_u(2,0)>0\,,\\
C(3,0)&=3I_s(3,0)-3I_u(3,0)\,,\\
C(2,1)&=\frac{\text{Disc}_s\mathcal{A}_u(\epsilon^2\Lambda^2,0)}{\pi(\epsilon^2\Lambda^2)^3}+I_s(2,1)-3I_u(3,0)+I_s(2,1)\,.
\end{aligned} \tag{3.18}$$

Due to positivity and the μ suppression in the integrands $I(n,m)$, we have the inequality,

$$I_{s,u}(n+1,m)<\frac{1}{\epsilon^2\Lambda^2}I_{s,u}(n,m)\,,$$

allowing us to construct positive quantities even when negative factors of the discontinuity integrals appear in the above expressions. From doing this we obtain the following linear positivity bounds,

$$C(2,0)>0\,,\quad C(3,0)+\frac{3}{\epsilon^2\Lambda^2}C(2,0)>0\,,\quad C(2,1)+\frac{3}{\epsilon^2\Lambda^2}C(2,0)-\frac{\text{Disc}_s\mathcal{A}_u(\epsilon^2\Lambda^2,0)}{\pi(\epsilon^2\Lambda^2)^3}>0\,. \tag{3.19}$$

JHEP06(2024)146

In the final line, the explicit factor of the discontinuity appears as a consequence of the t dependence of the lower limit of the u-channel integral in the dispersion relation. The discontinuity is positive and so serves to improve the strength of the positivity bounds if we are able to compute it in the EFT.

If we take arbitrary linear combinations of the first three dispersion relations in eq. (3.18), we can derive other positivity statements. In such a combination the coefficient of $C(2,1)$ must be positive for the combination to be positive, as it contains $I_s(2,1)$ which, if multiplied by a negative number cannot be compensated by anything in $C(2,0)$ or $C(3,0)$. Then we have a continuum of positive quantities parameterised by $\Omega, \Theta \in \mathbb{R}$,

$$C(2,1) - \frac{\text{Disc}_s\mathcal{A}_u(\epsilon^2\Lambda^2,0)}{\pi(\epsilon^2\Lambda^2)^3} + \Theta C(3,0) + \frac{\Omega}{\epsilon^2\Lambda^2}C(2,0) > 0\,, \quad \forall\,\Omega \geq 3\left|\Theta + \frac{1}{2}\right| + \frac{3}{2}\,. \tag{3.20}$$

Since $C(2,0)$ is positive, the strongest bound will be obtained when Ω takes its minimum value. The bound should be then satisfied for any Θ and so by varying over this parameter we find the equivalent statement,

$$|C(3,0)| < \frac{3}{\epsilon^2\Lambda^2}C(2,0) \quad \cup \quad C(2,1) - \frac{1}{2}C(3,0) + \frac{3}{2\epsilon^2\Lambda^2}C(2,0) - \frac{\text{Disc}_s\mathcal{A}_u(\epsilon^2\Lambda^2,0)}{\pi(\epsilon^2\Lambda^2)^3} > 0\,. \tag{3.21}$$

Finally, two further $C(n,m)$ coefficients we examine are,

$$\begin{aligned} C(4,0) &= 12I_s(4,0) + 12I_u(4,0) > 0\,, \\ C(3,1) &= 3I_s(3,1) - 3I_u(3,1) + 12I_u(4,0) - \frac{3\text{Disc}_s\mathcal{A}_u(\epsilon^2\Lambda^2,0)}{\pi(\epsilon^2\Lambda^2)^4}\,. \end{aligned} \tag{3.22}$$

We do not include $C(2,2)$ as it receives 1-loop corrections which are logarithmically divergent as $t \to 0^-$ [77, 92]. From these expressions we can derive, in a similar manner to before, the linear positivity bounds,

$$0 < C(4,0) < \frac{12}{(\epsilon^2\Lambda^2)^2}C(2,0) \quad \cup \quad C(3,1) + \frac{3}{\epsilon^2\Lambda^2}C(2,1) - \frac{3}{2\epsilon^2\Lambda^2}C(3,0) + \frac{9\,C(2,0)}{2(\epsilon^2\Lambda^2)^2} > 0\,. \tag{3.23}$$

3.3 Weak coupling assumption and low energy analyticity

All the above positivity bound statements can be applied to the various elastic photon amplitudes that were derived in section 3.1. These positivity bounds accounted for the presence of loops in the EFT, which would generate non-analyticities at arbitrarily low energy, due to the masslessness of the photon. In the three leading quantities $C(2,0)$, $C(3,0)$, and $C(2,1)$ the 1-loop corrections appear as polynomials in the Wilson coefficients and in particular do not introduce logarithms. At 2-loop or higher, it is possible for this to change and for logarithms to arise. Running loop corrections in quantities such as $C(4,0)$ and $C(3,1)$ (provided that they themselves do not diverge as $t \to 0^-$), which would take the form of logarithms [77], imply that the Wilson coefficients are dependent on the arbitrary dim-reg scale μ which can be chosen to be $\mu = \epsilon^2\Lambda^2$. With this choice of dim-reg scale the logarithmic corrections which depend on ratios of μ to $\epsilon^2\Lambda^2$, would vanish leaving some finite corrections.

JHEP06(2024)146

The assumption that loop corrections to the amplitude in the EFT are suppressed to the point of being negligible, either by a weak coupling in the UV (as for example in perturbative string theory) or a large hierarchy of scales (e.g. for gravitational interactions at low energies) is often termed *weak-coupling*. If we assume that the UV completion involves interactions that are controlled by a dimensionless coupling g_*^2 such that the EFT Lagrangian can be organised into a form exhibiting a single mass scale and the UV coupling (see for example [35, 91, 93, 94]):

$$\mathcal{L}_{\rm EFT} = \frac{1}{g_*^2}\Big(\Lambda^4 L_0(A/\Lambda, \partial/\Lambda) + g_*^2 L_1 + \dots\Big)\,, \tag{3.24}$$

then the loop counting parameter is effectively g_*^2. In this above expression the $L_{\mathfrak{L}}$ functions descend into the EFT from $\mathfrak{L}$-loop corrections in the UV theory. In fact from analysis of Feynman diagrams, one can determine that $\mathfrak{L}$-loop corrections are suppressed by a factor of $(g_*^2/16\pi^2)^{\mathfrak{L}}$, implying that the theory becomes strongly coupled (which in this context means a breakdown of the loop expansion) at $g_* = 4\pi$. As a consequence, if one assumes that $g_* \ll 1$, loop contributions and thus non-analyticities are suppressed throughout the regime of validity of the EFT and positivity bounds can be applied to the tree-level EFT amplitudes.

Finally, we note that even if $g_* > 4\pi$, there can be situations in which loop corrections in the EFT become suppressed by a large hierarchy of scales. One notable example of this is in the EFT of gravity, where power counting arguments reveal that loop corrections are ever-more suppressed by factors of $E/M_{\rm Pl}$ where E denotes a typical low-energy scale of the physical system, be it a scattering center of mass energy, or the curvature scale of the gravitational background [95]. This suppression however becomes weaker as E increases and so is less robust than the weakly-coupled UV scenario which remains accurate for all energies up to the cutoff.

In the weak-coupling approximation, non-analyticities in the amplitude start at the cutoff Λ_c which is generically higher than the scale explicit in the EFT action[3] $\Lambda_c^2 \gtrsim \Lambda^2$ and below this scale, the EFT amplitude is polynomial in Mandelstam variables. The corresponding dispersion relation exhibits branch cut integrals $I_{s,u}$ having lower limits starting at Λ^2. The upshot is that the assumption of weak coupling practically means we can set all loop contributions to zero as well as freely take $\epsilon \to 1$ from below. This also means that the explicit term involving the discontinuity evaluated at $\epsilon^2\Lambda^2$ is not present in the bounds. Whilst this assumption is not strictly necessary in our setup as we could in principle compute the 1-loop corrections, for the sake of comparison to causality bounds it is natural to neglect 1-loop corrections as the scattering time advance/delay is computed in the semi-classical regime.

Finally, we emphasise that our bounds do not rely on $s \leftrightarrow t$ (or triple) crossing symmetry in the form of null constraints. Such constraints have been fruitfully used in the numerical approach to positivity bounds to obtain optimal bounds on Wilson coefficients [41], however

[3]The scale explicitly appearing in the action Λ is where classically the effects of irrelevant interactions become comparable in strength to that of relevant and marginal interactions. This typically indicates the scale, at which tree-level perturbative unitarity breaks down at which point either loop corrections or new degrees of freedom must contribute to restore unitarity. If loop corrections do not restore unitarity, i.e. the unitarity breaking is non-perturbative in nature, then new degrees of freedom must arise at this scale, which we then identify as the *cutoff* of the EFT [96].

JHEP06(2024)146

when there is no mass gap there is no region in which fixed variable twice subtracted dispersion relations are valid in all scattering channels simultaneously (as would be the case within the Mandelstam triangle in a gapped theory). Our bounds rely only on validity of the fixed-t dispersion relation (for which low energy branch cuts can in principle be computed and subtracted to arbitrary precision) and are robust against low energy loop corrections.

3.4 Applying positivity bounds to the EFT: linear bounds

Ignoring loop corrections in the EFT then we find the above C coefficients to be,

$$\begin{aligned}
\Lambda^4 C(2,0) &= g_2 + f_2 \sin(2\theta)\sin(2\chi)\cos(\psi+\phi)\,,\\
\Lambda^6 C(3,0) &= 3g_3 \cos(2\theta)\cos(2\chi)\,,\\
\Lambda^6 C(2,1) &= \frac{1}{2}(-f_3 \sin(2\theta)\sin(2\chi)\cos(\psi+\phi) + 3g_3\cos(2\theta)\cos(2\chi) - 3g_3\\
&\quad - 4h_3(\sin(\theta)\cos(\theta)\cos(\phi) + \sin(\chi)\cos(\chi)\cos(\psi)))\,,\\
\Lambda^8 C(4,0) &= 12(2f_4 \sin(2\theta)\sin(2\chi)\cos(\psi+\phi) + g_4)\,,\\
\Lambda^8 C(3,1) &= 6(2f_4 \sin(2\theta)\sin(2\chi)\cos(\psi+\phi) + g_4) - 3(2g_4 + g_4')\cos(2\theta)\cos(2\chi)\,,
\end{aligned} \tag{3.25}$$

and the linear positivity bound statements allowing $\epsilon \to 1^-$ are,

$$g_2 + f_2 \sin(2\theta)\sin(2\chi)\cos(\psi+\phi) > |g_3 \cos(2\theta)\cos(2\chi)|\,, \tag{3.26}$$

$$\begin{aligned}
6g_2 > 6g_3 &+ 8h_3 \sin(\chi)\cos(\chi)\cos(\psi) + 8h_3 \sin(\theta)\cos(\theta)\cos(\phi)\\
&+ \sin(2\theta)\sin(2\chi)\cos(\psi+\phi)(-6f_2 + 2f_3)
\end{aligned} \tag{3.27}$$

$$f_2 \sin(2\theta)\sin(2\chi)\cos(\psi+\phi) + g_2 > 2f_4 \sin(2\theta)\sin(2\chi)\cos(\psi+\phi) + g_4 > 0\,, \tag{3.28}$$

$$\begin{aligned}
&\sin(2\chi)(2\sin(2\theta)(3f_2 - f_3 + 8f_4)\cos(\psi+\phi) - 4h_3\cos(\psi)) + 6g_2 + 8g_4\\
&\qquad > 6g_3 + 4(2g_4 + g_4')\cos(2\theta)\cos(2\chi) + 4h_3 \sin(2\theta)\cos(\phi)\,.
\end{aligned} \tag{3.29}$$

From the first inequality one can obtain the bounds on g_2 and f_2, namely

$$g_2 > 0\,, \quad g_2 > |f_2|\,. \tag{3.30}$$

Note that it is not possible to have $g_2 = 0$ in any unitary interacting theory, as g_2 can be expressed as an integral over a positive discontinuity which is non-zero if there are interactions. In fact it can be seen from the above bounds that if g_2 were to go to zero, all other Wilson coefficients under consideration would be forced to also vanish.

The dependence on angles makes it difficult in general to immediately read off the strongest constraints on the Wilson coefficients; however, two simple statements are

$$g_4 > 2|f_4|\,, \quad g_2 > |f_2 - 2f_4| + g_4\,. \tag{3.31}$$

Notice that the last inequality provides the upper bound on g_4, as can also be seen in the plots below.

Finally, whilst we find the bound (3.29), for the purposes of comparison to causality constraints we shall not impose it on the Wilson coefficients in the plots shown in this paper as the latter constraints are independent of g_4' as is explained below.

JHEP06(2024)146

3.5 Non-linear bounds

In the spirit of [40] we may use the Cauchy-Schwarz inequality to derive non-linear bound statements. One can define a normalised positive distribution from the s and u-channel discontinuities, then Cauchy-Schwarz inequality implies,

$$I_{s,u}(3,0)^2 < I_{s,u}(2,0)I_{s,u}(4,0)\,. \tag{3.32}$$

The latter term can be related to $C(2,0)C(4,0)$ resulting in the inequality

$$\frac{4}{3}C(3,0)^2 < C(2,0)C(4,0)\,. \tag{3.33}$$

In a similar way, one can derive the bound for $C(2,1)$,

$$C(2,1) - \frac{1}{2}C(3,0) = I_s(2,1) + I_u(2,1) - \frac{3}{2}(I_s(3,0) + I_u(3,0))\,. \tag{3.34}$$

The negative term on the right-hand side can be made positive by adding a larger quantity, again given by the Cauchy-Schwarz inequality,

$$(I_s(3,0) + I_u(3,0))^2 < (I_s(2,0) + I_u(2,0))(I_s(4,0) + I_u(4,0))\,. \tag{3.35}$$

The right-hand side of this inequality can be written in terms of $C(2,0)C(4,0)$ which leads us to the bound,

$$C(2,1) - \frac{1}{2}C(3,0) + \frac{\sqrt{3}}{4}\sqrt{C(2,0)C(4,0)} > 0\,. \tag{3.36}$$

In summary, we have the two non-linear bounds involving $C(4,0)$,

$$\frac{4}{3}C(3,0)^2 < C(2,0)C(4,0)\,, \quad \cup \quad C(2,1) - \frac{1}{2}C(3,0) + \frac{\sqrt{3}}{4}\sqrt{C(2,0)C(4,0)} > 0\,. \tag{3.37}$$

Given the inequality $0 < C(4,0) < 12C(2,0)/(\epsilon^2\Lambda^2)^2$, these two non-linear bounds are strictly stronger than the two linear bounds given in eq. (3.21).

In terms of EFT parameters, the two non-linear bounds are,

$$\begin{aligned}&(g_2 + f_2\cos(\phi+\psi)\sin(2\theta)\sin(2\chi))(g_4 + 2f_4\cos(\phi+\psi)\sin(2\theta)\sin(2\chi))\\ &> g_3^2\cos^2(2\theta)\cos^2(2\chi)\,,\end{aligned} \tag{3.38}$$

$$\begin{aligned}&3\sqrt{(g_2 + f_2\cos(\phi+\psi)\sin(2\theta)\sin(2\chi))(g_4 + 2f_4\cos(\phi+\psi)\sin(2\theta)\sin(2\chi))}\\ &> 3g_3 + 2h_3(\sin(2\theta)\cos\phi + \sin(2\chi)\cos\psi) + f_3\cos(\phi+\psi)\sin(2\theta)\sin(2\chi)\,.\end{aligned} \tag{3.39}$$

Notice that the last bound becomes the same as D^{stu} lower bound [40] for the full crossing symmetric choice of angles ($\phi = \psi,\ \chi = \theta = \pi/4$). The latter bound reads,

$$-\frac{3}{2}\sqrt{(g_2 + f_2\cos(2\phi))(g_4 + 2f_4\cos(2\phi))} < -\frac{1}{2}(3g_3 + 4h_3(\cos\phi) + f_3\cos(2\phi))\,. \tag{3.40}$$

JHEP06(2024)146

The upper D^{stu} derived in [40] can be formally applied to the photon EFT,

$$-\frac{1}{2}(3g_3+4h_3(\cos\phi)+f_3\cos(2\phi))<8\sqrt{(g_2+f_2\cos(2\phi))(g_4+2f_4\cos(2\phi))}\,. \tag{3.41}$$

However, this bound was consistently formulated only for gapped theories, as it relies on the full crossing symmetry for polynomial expansion of the amplitude. For gapless theories, the right-hand side of this bound will also include logarithmic terms which make it impossible to express the bound through $C(4,0)$.

Remarkably, the bounds (3.37) already result in restricting the values of $g_3,\ f_3,\ h_3$ to be in the compact ranges, regardless of the value of ϵ. Thus, these bounds do not rely on the assumption of weak coupling. Figure 3(a) shows that in the case $g_4=1$ these non-linear bounds coincide with the linear bound (3.21) for $\epsilon=1$. In general, these bounds provide stronger restrictions on the parameter space of the EFT, especially for smaller values of g_4, see figure 3(b).

3.6 Visualising positivity bounds

To visualise the regions of parameter space allowed by positivity bounds, we plot ratios of the Wilson coefficients with $g_2>0$. In other words, in what follows, if a Wilson coefficient g_n appears in the axis of a plot it is understood to represent the ratio g_n/g_2. To generate plots we use all linear and non-linear bounds given above *except* bound eqs. (3.29) and (3.41) and so we effectively have a six-dimensional space of ratios (since g_4' is not included in any bound), in which we select two-dimensional slices by fixing all but two of the Wilson coefficients. We do not include the positivity bound which depends on g_4' in our plots, as the purpose of our bounds is to compare with causality bounds which do not depend on this coefficient. However, from the view of *tree-level* positivity bounds there is nothing special about g_4' (other than that it vanishes in the forward limit) and it is expected to obey compact bounds just as the g_3, f_3, h_3 coefficients. These bounds however would depend on Wilson coefficients corresponding to higher order operators (just as the double sided bound on g_3 depends on g_4 etc.), beyond the order to which we work. When considering *loop* level contributions to the amplitude one should proceed with caution as the g_4' coefficient corresponds to the low energy quantity $\partial_s^2\partial_t^2\mathcal{A}$ which is divergent in the forward limit at 1-loop. Particularly, this divergence (and similar divergences in other higher derivative terms) has the potential to restrict which sum rules should be used in the numerical optimization approach to positivity bounds.

The positivity bounds we use to generate plots are unaffected by g_4' and so we effectively have a six-dimensional space of ratios, in which we select two-dimensional slices by fixing a number of Wilson coefficients. This is effectively equivalent to absorbing the value of g_2 into the scale appearing in the effective action, i.e. setting $g_2=1$.

As mentioned earlier, the positivity bounds above depend on several angular variables arising from the indefinite helicity of the incoming state, and in particular the bound holds for any value of these angles. Then, to find the strongest constraint on the Wilson coefficients, we must either vary over these angles or find a way to eliminate angles analytically and obtain the strongest bound as is described in appendix E. In the plots below we use a combination of these approaches.

JHEP06(2024)146

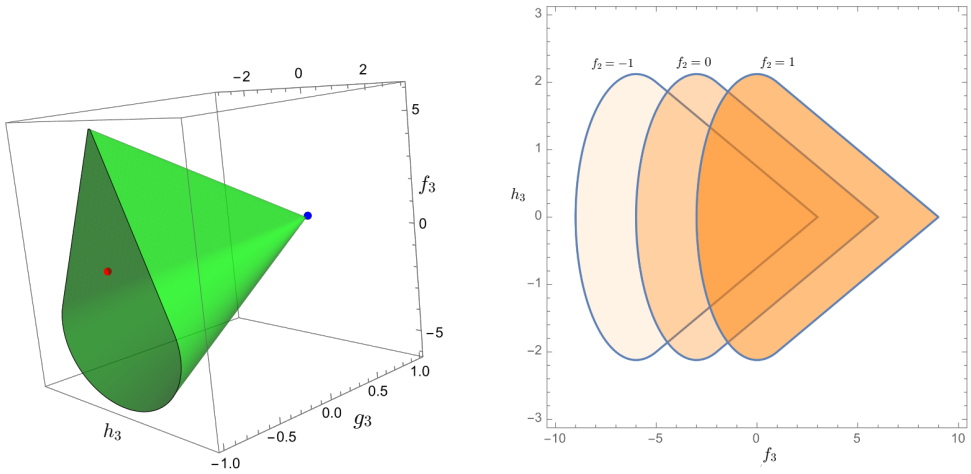

(a) (b)

Figure 2. (a) Allowed region for $g_3,\ f_3,\ h_3$ for $f_2 = 0,\ g_2 = 1,\ g_4 = 1,\ f_4 = 0$. The blue point corresponds to the scalar-axion UV completion (partial UV completion where both scalar and axion have the same coupling strength). The red point represents massive spin-2 (even II) UV completion. (b) $f_3 - h_3$ plots for $g_2 = 1,\ g_3 = -1$ and $f_2 = -1,\ 0,\ 1$. This bound does not depend on the values of $g_4,\ f_4$ and all other couplings in the EFT.

In figure 2(a) we take the slice of the bounds corresponding to $g_2 = g_4 = 1,\ f_2 = f_4 = 0$. We present the constraints on $g_3,\ f_3,\ h_3$ obtained analytically from linear inequalities after optimization with respect to angles. Even though the original inequalities (3.26) and (3.27)[4] are linear, the outcome of the optimization procedure described in appendix E leads to non-linear relations. The mixed axion-scalar UV completion, as well as massive spin-2 (even), lie precisely on the boundary of the allowed region. Figure 2(b) represents the $f_3 - h_3$ slices for different values of f_2.

In figure 3 we explore the correspondence between the two strongest linear bounds (3.26) and (3.27) derived under the assumption of weak coupling and the non-linear bounds (3.37) which do not rely on that assumption. We take $g_2 = 1,\ f_2 = f_4 = 0$. The left-hand panel shows the linear bounds after analytical optimization with respect to the angles, taking $\epsilon = 1$ (solid green cone) as well as the non-linear bounds (3.37) after numerical scanning over the angles (orange-shaded cone). The latter only deviates from the linear bounds by a small region which can be entirely attributed to the numerical error. As a non-trivial conclusion, non-linear bounds coincide with linear ones for $g_4 = 1$. If $g_4 < 1$, the non-linear bounds are stronger (recall that the linear bounds (3.26) and (3.27) do not depend on g_4). We plot the bounds (3.37) for different values of g_4. One can see that the allowed region is shrinking while keeping the same shape when g_4 is decreasing.

Last, figure 4 shows the bounds on the $f_4 - g_4$ plane following from (3.28) for $g_2 = 1$ at different values of f_2. Remarkably, the allowed region shrinks towards a line when the value of f_2 becomes close to ± 1. We save further analysis of positivity bounds for future work after the comparison with causality bounds.

[4]The other linear bounds are weaker than (3.26) and (3.27).

JHEP06(2024)146

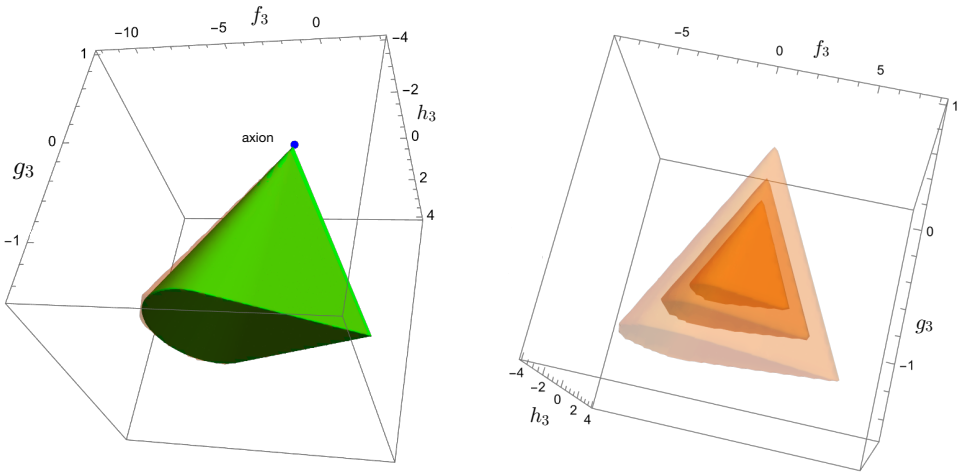

(a) (b)

Figure 3. (a) Allowed regions from analytically obtained linear ($\epsilon = 1$, green) bounds and numerical non-linear bounds of $g_3,\ f_3,\ h_3$ for $f_2 = -1$, $g_2 = 1$, $g_4 = 1$, $f_4 = -1/2$ (orange-shaded region). These two regions coincide upon a small computational error related to the non-optimal choice of angles in the numerical optimization of inequalities. The blue point corresponds to the axion partial UV completion. (b) Non-linear bounds of $g_3,\ f_3,\ h_3$ for $g_2 = 1$, $f_2 = 0$, $f_4 = 0$ and for different values of $g_4 = 1,\ 1/2,\ 1/4$. The inner region corresponds to the lowest value of g_4.

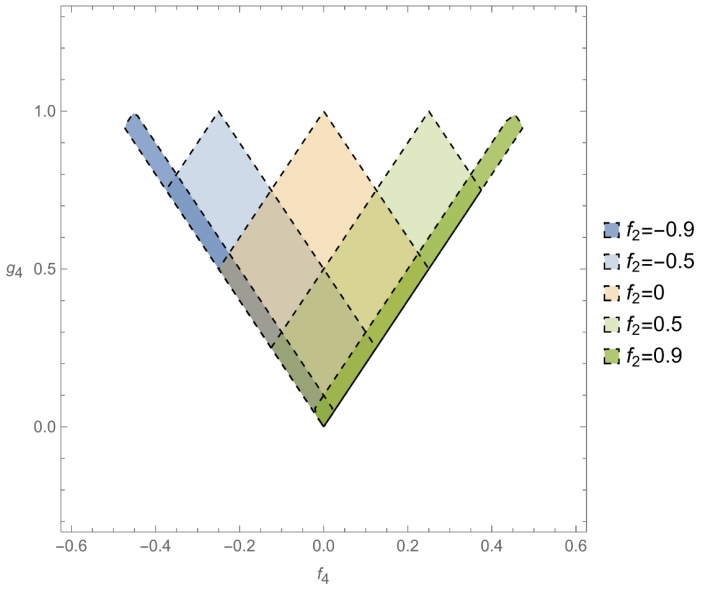

Figure 4. Positivity bounds in the $f_4 - g_4$ plane with Wilson coefficients set to $g_3 = f_3 = h_3 = 0$, varying f_2. As the value of $f_2 \to 1$ the allowed region approaches the line segment going from $(f_4, g_4) = (0, 0)$ to $(0.5, 1)$ and similarly as $f_2 \to -1$ approaches the line segment going from $(f_4, g_4) = (0, 0)$ to $(-0.5, 1)$.

JHEP06(2024)146

4 Causality bounds

In this section, we analyze bounds arising on the Wilson coefficients of the photon EFT from a related, but different perspective than in the previous sections. Here, we will obtain bounds by imposing causal propagation of the two physical photon modes around a non-trivial electromagnetic background. This is a purely low-energy calculation and does not rely any specific assumptions on the UV completion of the theory. We will follow the analysis performed in [69] for a scalar field theory. More specifically, we will consider the propagation of a linearized mode around a spherically-symmetric electromagnetic background in the regime where the scale measuring the variations of the background is much larger than the scale at which the perturbative mode varies. This will allow us to compute the time delay experienced by the mode traveling on a non-trivial background compared to that of a mode traveling in a background with $F_{\mu\nu} = 0$. Causal propagation dictates that the time delay is bounded as

$$\Delta T > -1/\omega\,, \tag{4.1}$$

where ω is the frequency of the mode. This simply indicates that one should not have a measurable time advance.

4.1 Spherically-symmetric backgrounds

To proceed we compute the equations of motion (explicitly shown in appendix A) and consider small fluctuations $\mathcal{A}_\mu$ on top of a background $\bar{A}_\mu(r)$ such that, in spherical coordinates,

$$A_\mu(t, r, \theta, \varphi) = \bar{A}_\mu(r) + \mathcal{A}_\mu(t, r, \theta, \varphi)\,, \tag{4.2}$$

where the spherically-symmetric background is given by[5]

$$\bar{A}_\mu(r)\mathrm{d}x^\mu = \bar{A}_0(r)\mathrm{d}t\,. \tag{4.3}$$

We assume that this background is sourced by an arbitrary, spherically-symmetric, external current J^ν. One is then left with the task to expand the vector perturbations in spherical harmonics. In order to do so, we will assume azimuthal symmetry and thus neglect any φ dependence, meaning that we effectively take the quantum number m to be vanishing and then the spherical harmonics reduce to Legendre polynomials instead. We will also assume that the time dependence factorises out in the form $e^{i\omega t}$ where ω is the frequency of the wave. We parameterise the gauge field as

$$\mathcal{A}_\mu(t, r, \theta) = \frac{1}{r}\sum_{I=1}^{4}\sum_{\ell\geq 0} D_I^\ell(r) Z_\mu^{(I)\ell}(\theta) e^{i\omega t}\,, \tag{4.4}$$

[5]Note that a radial component that depends only on r could be included but this is just a gauge mode that does not contribute to the field strength.

JHEP06(2024)146

where we take the basis

$$
\begin{aligned}
Z_\mu^{(1)\ell} &= \delta_\mu^t Y_\ell(\theta)\,, \\
Z_\mu^{(2)\ell} &= \delta_\mu^r Y_\ell(\theta)\,, \\
Z_\mu^{(3)\ell} &= \frac{r}{\sqrt{\ell(\ell+1)}}\delta_\mu^\theta \partial_\theta Y_\ell(\theta)\,, \\
Z_\mu^{(4)\ell} &= \frac{r}{\sqrt{\ell(\ell+1)}}\sin\theta\delta_\mu^\varphi \partial_\theta Y_\ell(\theta)\,.
\end{aligned}
\tag{4.5}
$$

The functions $Y_\ell(\theta)$ are the usual Legendre polynomials and ℓ denotes the order of a given partial wave. The functions $Z_\mu^{(I)\ell}$ with $I = 1, 2, 3$ have polar or even parity, whereas $I = 4$ has axial or odd parity.[6] It follows that the perturbation modes $D_I^\ell(r)$ are also real and inherit polar parity for $I = 1, 2, 3$ and axial parity for $I = 4$, meaning that those two sectors decouple at leading order. One of the D_I^ℓ modes can be removed straightforwardly via a gauge transformation of the form $A_\mu \to A_\mu + \partial_\mu\chi$ with

$$
\chi(t, r, \theta) = -\frac{D_3^\ell(r)}{\sqrt{\ell(\ell+1)}} Y_l(\theta) e^{i\omega t}\,. \tag{4.6}
$$

We can now consider the redefinition

$$
\begin{aligned}
u_1^\ell &\equiv D_1^\ell - \frac{i\omega r}{\sqrt{\ell(\ell+1)}} D_3^\ell\,, \\
u_2^\ell &\equiv \frac{1}{r}\left(D_2^\ell - \frac{r}{\sqrt{\ell(\ell+1)}}(D_3^\ell)'\right), \\
u_4^\ell &\equiv D_4^\ell\,,
\end{aligned}
\tag{4.7}
$$

so that the vector perturbations take the following form

$$
\mathcal{A}_\mu = \left(\frac{u_1^\ell}{r} Y_\ell, u_2^\ell Y_\ell, 0, \frac{u_4^\ell}{\sqrt{\ell(\ell+1)}}\sin\theta Y_l'\right) e^{i\omega t}\,. \tag{4.8}
$$

Note that we have introduced a $1/r$ factor in the definition of u_2^ℓ which makes this function dimensionful, however, this will simplify further analysis. By analyzing the equations of motion, one can further notice that one of them corresponds to a constraint that removes the remaining unphysical degree of freedom and we are left only with two propagating modes (given by u_2^ℓ and u_4^ℓ) as expected for a massless vector field in 4 dimensions. This constraint equation sets a linear combination of u_1^ℓ, u_2^ℓ, and derivatives of u_2^ℓ to zero and can be found at any desired order in the EFT expansion. The explicit expression is given in eq. (A.3).

We can solve the equations of motion for the 2 remaining physical degrees of freedom, u_2^ℓ and u_4^ℓ, by removing higher-order radial derivatives iteratively in order to obtain a second-order differential equation for each mode and using the WKB approximation. We work with $\ell > 0$ since a vector field does not propagate a monopole mode.[7] In this case, it is well-known

[6] The parity of each mode can be understood by their behavior under a space inversion $\theta \to \pi - \theta$. Under this transformation we have $\left(Z_\mu^{(1,2,3)\ell}, Z_\mu^{(4)\ell}\right) \to \left((-1)^\ell Z_\mu^{(1,2,3)\ell}, (-1)^{\ell+1} Z_\mu^{(4)\ell}\right)$.

[7] While this is a well known fact, it can be seen explicitly in our setting by setting $\ell = 0$ in the equations of motion in which case we are left with only two modes, namely D_1^0 and D_2^0. One of this modes can be removed by a gauge transformation $\chi(t, r, \theta) = -D_1^0(r) Y_0 e^{i\omega t}/(i\omega r)$. Meanwhile, the second one is set to zero by Maxwell's equations. Thus there are no propagating modes.

JHEP06(2024)146

that we need to take $r \to e^{\rho}$ to better describe the problem at low ℓ [97]. Once the equations of motion are expressed in this variable, we can remove the friction term and then change variables back to r. For more detail on how to perform this calculation see [69, 74]. We now proceed to solve the equations of motion for the two physical degrees of freedom by using the WKB approximation to find the phase shift experienced by these modes when propagating around non-trivial backgrounds.

Regime of validity of the EFT and WKB approximation. Following the same notation as in [69], i.e. we denote by r_0 the typical oscillation length of the background $\bar{A}_0(r)$ and by $\bar{\Phi}_0$ its typical amplitude, which carries mass dimensions. We also introduce the reduced (dimensionless) radial coordinate R defined as

$$\bar{A}_0(r) = \bar{\Phi}_0 f(R)\,, \quad R \equiv \frac{r}{r_0}\,. \tag{4.9}$$

The impact parameter of the free theory is designated by b, and its reduced partner B

$$\omega b = \ell + 1/2\,, \qquad B \equiv \frac{b}{r_0}\,. \tag{4.10}$$

The strongest bounds that we will find will be in two different regimes. One for small B which is akin to wave like scattering and the other one for $B \gg 1$ which is similar to the eikonal regime calculations from scattering amplitudes. Both regimes arise in different regions of the Wilson coefficients space. In order to stay within the regime of validity of the EFT, we following parameters need to remain small

$$\epsilon_1 \equiv \frac{\bar{\Phi}_0}{r_0\Lambda^2} \ll 1\,, \qquad \epsilon_2 \equiv \frac{1}{r_0\Lambda} \ll 1\,, \qquad \Omega\ \epsilon_2 \equiv \frac{\omega}{r_0\Lambda^2} \ll 1\,. \tag{4.11}$$

Furthermore, we will take $\epsilon_1 \ll \epsilon_2$ to neglect the ϵ_1^4 contributions and $\omega r_0 \gg 1$ as well as $\Omega > 1$ to ensure the consistency of our expansion within the WKB approximation. The former is simply the requirement for the WKB approximation to hold and tells us that the typical scale of variation of the perturbation is shorter than that of the background. The latter ($\Omega > 1$) is required so that higher WKB corrections which cannot be included consistently in the phase shift calculation can be ignored at the order we work at. Overall, this requires the following hierarchy for our parameters

$$\epsilon_1 \ll \epsilon_2 \ll 1 < \Omega \ll \frac{1}{\epsilon_2}\,. \tag{4.12}$$

This hierarchy and the order of magnitude of the operators we considered can be observed in figure 5. It is also worth mentioning that this EFT power counting uses the standard assumption that the Wilson coefficients are order one. If the Wilson coefficients were allowed to become uncontrollably large, the cutoff would effectively be smaller, leading to an earlier breaking of the EFT expansion.

Time delay. Now that we have all the ingredients, we can apply the machinery to get the phase shift and then the time delay. The phase shift experienced by the propagating

JHEP06(2024)146

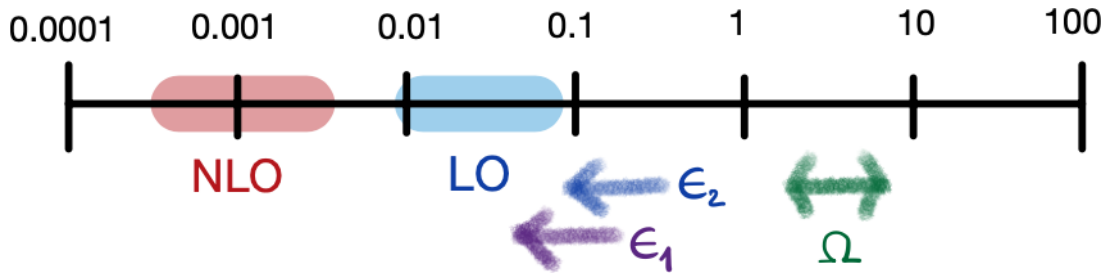

Figure 5. Schematic depiction of the order of magnitude of the expansion parameters in eq. (4.11) and the operators in the EFT. The LO label corresponds to the leading order terms in the EFT expansion that are considered in this work, that is, operators with contributions of order $\epsilon_1^2, \epsilon_1^2\epsilon_2^2$, and $\epsilon_1^2\epsilon_2^2\Omega^2$. Meanwhile, the NLO area corresponds to operators at next to leading order that we compute and ensure are suppressed. These are contributions of order $\epsilon_1^4, \epsilon_1^2\epsilon_2/\Omega^2, \epsilon_1^2\epsilon_2^4, \epsilon_1^2\epsilon_2^4\Omega^2, \epsilon_1^4\epsilon_2^2$, and $\epsilon_1^4\epsilon_2^2\Omega^2$.

modes can be found by using the WKB approximation to solve their equations of motion, which are given by

$$u_I^\ell(R)'' = -W_{I,\ell}(R)u_I^\ell\,, \qquad \text{for } I = 2, 4\,, \tag{4.13}$$

where the explicit expressions for $W_{I,\ell}(R)$ can be found in eq. (B.1) and eq. (B.2). Note that we slightly abuse the notation in the above expression by including the field u_I^ℓ when in fact we are now describing the evolution of the field-redefined u_I^ℓ such that their respective equations of motion are free of any friction terms. The phase shift is found by looking at the behavior of the solution at infinity, that is, $\lim_{r\to\infty} u_I^\ell \propto \left(e^{2i\delta_{I,\ell}}e^{i\omega r} - e^{i\pi\ell}e^{-i\omega r}\right)$. Thus, the phase-shift takes the following form

$$\delta_{I,\ell}(\omega) = (\omega r_0)\left[\int_{R^t_{I,\ell}}^{\infty} \frac{U_{I,\ell}(R)}{\sqrt{1-\left(\frac{R^t_{I,\ell}}{R}\right)^2}}\mathrm{d}R + \frac{\pi}{2}\left(B - R^t_{I,\ell}\right)\right], \tag{4.14}$$

where $R^t_{I,\ell}$ is the turning point for the degree of freedom u_I^ℓ defined by $W_{I,\ell}(R^t_{I,\ell}) = 0$ and $U_{I,\ell}$ is such that

$$\sqrt{W_{I,\ell}(R)} = \sqrt{1-\left(\frac{R^t_{I,\ell}}{R}\right)^2} + \frac{U_{I,\ell}(R)}{\sqrt{1-\left(\frac{R^t_{I,\ell}}{R}\right)^2}}\,. \tag{4.15}$$

The explicit expression for all the functions appearing in this section can be found in appendix B. Note that we perform an expansion around the turning point in a way as to ensure the convergence of the integral. In particular, we have $U_{I,\ell}(R^t_{I,\ell}) = 0$. Furthermore, it is easy to show that $U_{I,\ell} = \mathcal{O}(\epsilon_1^2)$ and $R^t_{I,\ell} = B + \mathcal{O}(\epsilon_1^2)$, hence the turning point can safely be replaced by its leading-order value B since any corrections would contribute to $\mathcal{O}(\epsilon_1^4)$ which can be neglected in the expansion scheme we have chosen. The phase shift then reads

$$\delta_{I,\ell}(\omega) = (\omega r_0)\left[\int_{B}^{\infty} \frac{U_{I,\ell}(R)}{\sqrt{1-\frac{B^2}{R^2}}}\mathrm{d}R + \frac{\pi}{2}\left(B - R^t_{I,\ell}\right)\right]. \tag{4.16}$$

JHEP06(2024)146

From there, obtaining the time delay from the phase-shift is then straightforward,

$$(\omega \Delta T_{b,I,\ell}(\omega)) = 2\omega \frac{\partial \delta_{I,\ell}(\omega)}{\partial \omega}\Big|_b = 2(\omega r_0)\left[\int_B^\infty \frac{\partial_\omega(\omega U_{I,\ell}(R))}{\sqrt{1-\frac{B^2}{R^2}}}\mathrm{d}R + \frac{\pi}{2}\Big(B - \partial_\omega\Big(\omega R^t_{I,\ell}\Big)\Big)\right], \tag{4.17}$$

where $|_b$ means that we perform the derivative at fixed impact parameter b, that is, we replace $\ell = \omega b - 1/2$ and then perform the ω derivative. This setup resembles the scattering of a particle off a fixed background.

4.2 Causality bounds

In this section, we will work with the scattering amplitudes parameters in eqs. (2.4), instead of the Wilson coefficients of the Lagrangian in eq. (2.3). This will allow for a straightforward comparison with the positivity bounds in the previous section.

In order to find the causality bounds, we impose the requirement that we cannot get a resolvable time advance, that is, that eq. (4.1) is satisfied for both even and odd sectors with the time delay given by eq. (4.17). The precise method has been described in previously in [69] and is summarized for completion in appendix C.

Sign-definite contributions. We will now investigate the contribution to the time delay from the different scattering amplitude parameters, in both the even and odd sector. In particular, we identify the ones that are sign-definite as this will lead us to predict whether the causality bounds will be one-sided or compact. The results can be found in table 2. First, we define the following positive integrals

$$\mathcal{A}^+ = 2(\omega r_0)B^2\int_B^\infty \frac{(f'(R)/R)^2}{\sqrt{1-B^2/R^2}} > 0\,, \tag{4.18}$$

$$\mathcal{B}^+ = 2(\omega r_0)\int_B^\infty \frac{B^2}{R^2}\frac{(f'(R)/R - f''(R))^2}{\sqrt{1-B^2/R^2}} > 0\,, \tag{4.19}$$

$$\mathcal{C}^+ = 2(\omega r_0)\int_B^\infty \frac{B^2}{R^2}\sqrt{1-B^2/R^2}\left(\frac{f'(R)}{R} - f''(R)\right)^2 > 0\,. \tag{4.20}$$

We also introduce the following (non sign-definite) integral for convenience,

$$(\omega \Delta T^{(f_3)}_{b,4,\ell}(\omega)) = -\frac{2}{3}(\omega r_0)\epsilon_1^2\epsilon_2^2\int_B^\infty \frac{B^2}{R^2}\frac{\left[\frac{f'(R)^2}{R^2} - (f''(R)^2 + f'(R)f^{(3)}(R))\right]}{\sqrt{1-B^2/R^2}}\,. \tag{4.21}$$

For concreteness, we work with a localized background of the form

$$f(R) = \left(\sum_{n=0}^{p} a_{2n}R^{2n}\right)e^{-R^2}\,, \tag{4.22}$$

where the coefficients a_{2n} are taken to be at most of order 1. This ensures that the background and all its derivatives are under control. For simplicity, we will restrict ourselves to the case where the power of the polynomial is $p = 3$, which provides sufficient freedom to derive relatively strong bounds. This background corresponds to an electric field in the radial direction. At leading order the equations of motion for the background read, $\partial_r^2 A_t = J^t = \rho$,

JHEP06(2024)146

Wilson coefficient	$(\omega\Delta T_{b,2,\ell}(\omega))$	$(\omega\Delta T_{b,4,\ell}(\omega))$	Sign-definiteness
f_2	$\epsilon_1^2\mathcal{A}^+ > 0$	$-\epsilon_1^2\mathcal{A}^+ < 0$	No
g_2	$\epsilon_1^2\mathcal{A}^+ > 0$	$\epsilon_1^2\mathcal{A}^+ > 0$	(+)
f_3	$-\frac{1}{3}\epsilon_1^2\epsilon_2^2\mathcal{B}^+ < 0$	$\omega\Delta T^{(f_3)}_{b,4,\ell}(\omega)$	No
g_3	$-\epsilon_1^2\epsilon_2^2\mathcal{B}^+ < 0$	$-3(\omega\Delta T^{(f_3)}_{b,4,\ell}(\omega))$	No
h_3	non sign-definite	$4(\omega\Delta T^{(f_3)}_{b,4,\ell}(\omega)) + 2\epsilon_1^2\epsilon_2^2\frac{\mathcal{A}^+}{B^2}$	No
f_4	$24\epsilon_1^2\epsilon_2^2\Omega^2\mathcal{C}^+ > 0$	$-24\epsilon_1^2\epsilon_2^2\Omega^2\mathcal{C}^+ < 0$	No
g_4	$12\epsilon_1^2\epsilon_2^2\Omega^2\mathcal{C}^+ > 0$	$12\epsilon_1^2\epsilon_2^2\Omega^2\mathcal{C}^+ > 0$	(+)
g_4'	0	0	0

Table 2. Contributions to the time delay in the odd and even sectors from various Wilson coefficients.

where ρ is a localized electric charge density of order $\frac{\Phi_0}{r_0^2}$ and our choice of profile $f(R)$ defines the specific profile of the charge density. Notice that it is physical to have both negative and positive contributions as long as we work with an analytic function since this is an electric charge density. Higher-order EFT contributions to the background equation of motion simply give small corrections to the charge density configuration. Furthermore, note that the expansion scheme we have chosen is such that the final time delay is linear in *all* scattering amplitude parameters and hence we have

$$(\omega\Delta T_{b,I,\ell}(\omega)) = \sum_J \mathcal{W}_J(\omega\Delta T^{(J)}_{b,I,\ell}(\omega))\,, \tag{4.23}$$

where the Wilson coefficients are denoted by $\mathcal{W}_J$ and the index J runs from 1 to 8 such that $\mathcal{W}_J = \{f_2, g_2, f_3, g_3, h_3, f_4, g_4, g_4'\}_J$ (even though we will see that the time delay does not depend on g_4' in either sector), and where $\Delta T^{(J)}_{b,I,\ell}$ are numerical factors depending on $\epsilon_1, \epsilon_2, \Omega, B, a_0, a_2, a_4$, and a_6 but *not* on the Wilson coefficients $\mathcal{W}_J$.

We can see from table 2 that the time delay is *independent* of g_4' and that the coefficients g_2 and g_4 produce sign-definite contributions to the time delay across both even and odd sectors. Any two-dimensional bound that does not involve g_2 and g_4 will be a two-sided bound that can lead to a compact causal region. In the following we show several representative two-dimensional bounds. First we analyze the f_2 and g_2 case which will allows us to fix the value of g_2. For the other bounds, we plot a two-dimensional slice of whole $6d$ parameter space $f_2, f_3, g_3, h_3, f_4, g_4$, that is, we fix the value of four of those coefficients and plot the bounds on the other two.

4.2.1 Two-dimensional bounds

Bounds on f_2 and g_2. It is possible to obtain the strongest bounds on the leading order Wilson coefficients by considering a regime of validity of the EFT and WKB approximation in which all higher order corrections are highly suppressed. Instead of the hierarchy for the parameters in eq. (4.12), we can take $\epsilon_2 \ll \epsilon_1 \ll 1$. Within this setting, one can show that

$$(\omega\Delta T_{b,I,\ell}(\omega)) = \epsilon_1^2 X_I\mathcal{A}^+ + \mathcal{O}(\epsilon_1^2\epsilon_2^2, \epsilon_1^2\epsilon_2^2\Omega^2)\,, \tag{4.24}$$

JHEP06(2024)146

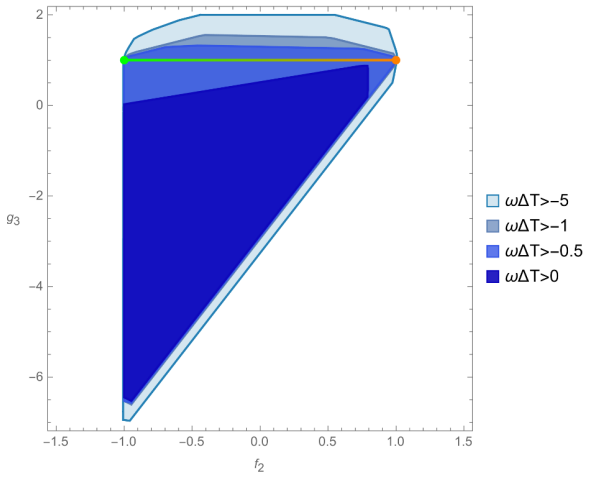

Figure 6. Causality bounds in the (f_2, g_3)-plane for $f_3 = 3f_2$, $h_3 = 0$, $f_4 = f_2/2$, and $g_4 = 1$ which are consistent with the values of the scalar and axion partial UV completions. One can see that the points denoting the values of the partial UV completions, scalar in green and axion in orange, lie in the boundary of the region $\omega\Delta T > -a$, for $a = 0.5, 1, 5$. The line connecting them involves values of a partial UV completion involving both the scalar and axion. We show alternative bounds for a different constraint on the time delay. Depending on how negative we allow the time delay to be, we obtain weaker or stronger bounds. More importantly, if we were to require strict positivity of the time delay, this would rule out the axion and scalar partial UV completions, which indeed are causal.

where

$$X_I = \begin{cases} g_2 + f_2 & \text{for } I = 2\,, \\ g_2 - f_2 & \text{for } I = 4\,. \end{cases} \tag{4.25}$$

Thus one can easily see that the time delay is sign-definite for both modes at leading order. The causality constraint $(\omega\Delta T_{b,I,\ell}(\omega)) > -1$ translates into $X_I > -1/(\epsilon_1^2 \mathcal{A}^+) \sim -1/((\omega r_0)\epsilon_1^2)$ where $(\omega r_0)\epsilon_1^2 = \Omega\epsilon_2(\epsilon_1/\epsilon_2)^2$ can be made arbitrarily large for $\epsilon_2 \ll \epsilon_1$ and hence we get

$$g_2 + f_2 > 0\,, \qquad g_2 - f_2 > 0\,. \tag{4.26}$$

Together, this imply that g_2 is positive. Note that this constrain includes the predictions from the low energy limit of string theory in four dimensions [98] in which $f_2 = 0$ since all the EFT corrections are proportional to powers of $T_{\mu\nu}T^{\mu\nu}$, where $T^{\mu\nu}$ is the stress-energy tensor of the photon.

From now on, we will set $g_2 = 1$ which simply fixes the cutoff scale of the EFT to be determined solely by Λ. The $g_2 = 0$ case will be treated separately at the end of this section.

Bounds on f_2 and g_3. As a first illustrative example, we focus on the bounds obtained in the (f_2, g_3)-plane. In that case, there won't be any sign-definite contributions across both even and odd sectors in the, which allows for compact bounds, but we get one-sided bounds from the even sector, which can easily be explained.

Starting with the scalar and axion UV completion as depicted in figure 6, we have both f_3 and f_4 that are proportional to f_2 to allow for a smooth transition between the scalar and axion UV completions. The line corresponds to a partial UV completion involving an

JHEP06(2024)146

axion and a scalar whose coefficients are simply the sum of the axion and scalar cases with a parameter (namely f_2 in this case) tuning the contribution from each. More precisely, the coefficients in this line are given by

$$\mathcal{W}_J = \cos\theta\ \mathcal{W}_J^{\text{scalar}} + \sin\theta\ \mathcal{W}_J^{\text{axion}}\,, \quad \theta \in [0, \pi/2]\,, \tag{4.27}$$

so that at $\theta = 0$ we have the purely scalar case and at $\theta = \pi/2$ we have the purely axionic case. The line precisely lies within our causality bounds whereas the scalar and axion UV completions exactly sit on the boundary.

Along this line joining the scalar and axion UV completions, we set f_3 and f_4 to be proportional to f_2 and hence we have a time delay in the form of $(\omega\Delta T^{(f_2)} + 3\omega\Delta T^{(f_3)} + \omega\Delta T^{(f_4)}/2)f_2 + \omega\Delta T^{(fg_3)}g_3 + (\text{constant})$. Interestingly, the term multiplying f_2 is strictly positive in the even sector, whereas the one in front of g_3 is negative. When imposing the causality constraint we end up with an equation of the form $g_3 < (\text{positive})f_2 + (\text{constant})$ and hence the even sector is responsible for the top and/or left bounds (the same configuration will arise in the (f_2, f_3)-plane in figure 6), whereas we obtain the rest of the compact region thanks to the less rigid structure in the odd sector. Both UV partial completions and the whole line joining them are exactly contained within our causality bounds.

In figure 6, we also plot alternative bounds on the time delay in order to appreciate how the boundary of the causal region changes. Our causality bound requires $\omega\Delta T > -1$, if instead, we allow for a more negative time delay, the bounds would slightly weaken as expected. Similarly, the bound get stronger if we force the time delay to be less negative. It is clear from figure 6 that if we require strict positivity of the time delay, that is, $\omega\Delta T > 0$, then we would rule-out well behaved partial UV completions. This shows that strict positivity is too strong of a requirement and in fact, would rule out known causal theories. Although we show this only for a two-dimensional slice of the parameter space, this can be shown to be a generic feature for all slices.

Let us now turn to the 1-loop QED case in figure 8 where three different sets of coefficients are known to correspond to the scalar, spinor, and vector UV completions, as given in table 1. For each case independently, we leave f_2 and g_3 arbitrary and set the other values so that they match the ones of the relevant UV completion. It is clear that the structure is the same, as in the left and/or top bounds seen in figure 7 come from the even sector whereas the right and bottom ones arise from the odd sector.

It is interesting to note that the causality bounds for the three sets of different (f_3, h_3, f_4, g_4) coefficients corresponding to the values they take in the scalar, spinor and vector one-loop QED partial UV completions are very similar. In fact, there is no noticeable difference in the even sector bounds. One main difference however is the lower bound, coming from the odd sector. It has the same slope for all three but is noticeably less constraining in the vector case. To understand this, let us turn to the generic equation governing such constraints. The slope is given by the coefficients of f_2 and g_3, but the vertical displacement of the bound is linear in $\sum_J \mathcal{W}_J(\omega\Delta T^{(J)}_{b,I,\ell}(\omega))$ where J runs over the fixed values of (f_3, h_3, f_4, g_4). From our analysis, we see that it is the h_3 contribution that is responsible for the discrepancy between the vector case and the other two. Let us focus on this and keep aside the other Wilson

JHEP06(2024)146

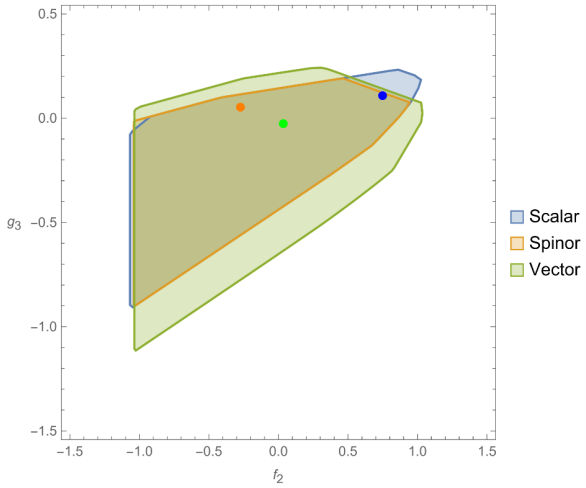

Figure 7. Causality bounds in the (f_2, g_3)-plane for various values of (f_3, h_3, f_4, g_4) that are consistent with the scalar, spinor and vector QED partial UV completions, respectively in blue, orange, and green, and are given in table 1. It is important to note that the three bounds are superimposed but each is derived for different values of (f_3, h_3, f_4, g_4). Just as an indication, we have approximately $(f_3, h_3, f_4, g_4) \sim (0.36, 0.04, 0.01, 0.10)$ for the scalar, $(-0.13, -0.01, 0.00, 0.02)$ for the spinor and $(0.02, 0.00, 0.00, 0.01)$ for the vector.

coefficients for now. Then, the equation for the lower bound is given by

$$g_3 > (\text{positive}) f_2 + \mathcal{H}_3 h_3 + (\text{constant}) \,, \tag{4.28}$$

where the numerical factor $\mathcal{H}_3$ is optimised such that the combination $\mathcal{H}_3 h_3$ is maximised for a tighter bound. This in turn means that the vertical position of the lower bound only depends on the absolute value $|\mathcal{H}_3 h_3|$. Turning now to table 1, it is easy to see that the value for $|h_3|$ is an order of magnitude smaller in the vector case than both the scalar and spinor and hence, this explains the fact that causality is less constraining in the vector case. There is also a noticeable difference in the bounds on the top right corner which again comes from the odd sector. In this case, the upper bound on g_3 is of the form

$$g_3 < (\text{negative}) f_2 + (\text{positive})(f_3 + 4h_3) + (\text{positive}) h_3 + (\text{positive})(g_4 - 2f_4) + (\text{constant}) \,, \tag{4.29}$$

where all the contributions from the parameters different from f_2 are positive and make the bound weaker. For the scalar QED, the values of the parameters in front of the positive definite contributions are positive and larger than in the spinor and vector QED cases so the bound is weaker in that case. For $f_2 \leq 0.5$ the bound is dominated by the even sector constraints so we have no large difference in the bounds.

Last, we analyze tree-level UV completions involving spin-2 fields. More precisely, we will look into the partial UV completions constructed in [75–77]. The spin-2 partial UV completion in [75] is constructed by integrating out a massive spin-2 with a minimal coupling to the photon, that is, a coupling $h_{\mu\nu} T^{\mu\nu}$ where $T^{\mu\nu}$ is the stress-energy tensor of the photon. Meanwhile, the partial UV completions in [77] are constructed by on-shell amplitude methods and requirements on the Regge behaviour. We can see that these partial UV completions lie

JHEP06(2024)146

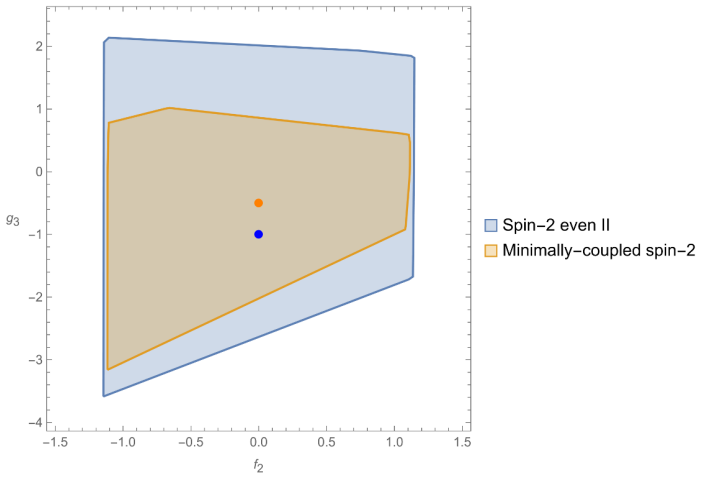

Figure 8. Causality bounds in the (f_2, g_3)-plane with all other coefficients set to the values of the corresponding partial UV completions as in table 1. Precisely, we have $f_3 = h_3 = f_4 = 0$ for both and $g_4 = 1$ and $1/2$ for the blue and orange regions respectively. We see that the partial UV completions lie within the causal region. Note that the spin-2 even II partial UV completion is related to the minimally coupled graviton one by rescaling g_2 by a factor of 2 and keeping all other parameters unchanged.

within our causal region. There are additional partial UV theories constructed in [77] that involve non-minimal couplings and are not consistent with causality which is not surprising in itself as these partial UV theories are not expected to admit a consistent full UV completion in the first place. We defer the analysis of those theories to appendix D.

Bounds on f_2 and f_3. Neither f_2 nor f_3 contribute in a sign-definite way to the total time delay (see table 2) over both even and odd sectors and hence there are no obvious one-sided bounds. This freedom is welcome as it allows for compact causality regions in the (f_2, f_3)-plane as can be seen in figure 9.

To better understand these bounds, we can analyse the even and odd sectors separately. Note that we have set $f_4 = f_2/2$ so that one can use f_2 as a dialing parameter to extrapolate between the scalar and axion UV completions, as can be seen in figure 9. The time delay now reads $(\omega\Delta T^{(f_2)} + \omega\Delta T^{(f_4)}/2)f_2 + \omega\Delta T^{(f_3)} f_3 + (\text{constant})$ with the terms multiplying f_2 and f_3 in this expression being respectively strictly positive and negative in the even sector, similarly to the previous (f_2, g_3) analysis. This means that the even sector will provide upper and/or left bounds depending on the magnitude of the positive slope, $f_3 < (\text{positive})f_2 + (\text{constant})$. When carefully processing the bounds, we confirm that the left and top bounds come from the even sector, whereas the odd sector has a richer structure and produces the remaining constraints, hence explaining the hard changes of slopes on the right side.

Once again, we plot the whole line joining the scalar and axion UV completion points, parametrized by f_2 going from 1 to -1, in figure 9. We have the same qualitative behavior, i.e. the end points corresponding to the scalar and axion UV completions are on the boundary of the causality bounds whereas the rest of the line is within.

Bounds on f_2 and h_3. When going to the (f_2, h_3)-plane, we choose to set all remaining coefficients in such a way that they can satisfy either the scalar or the axion partial UV

JHEP06(2024)146

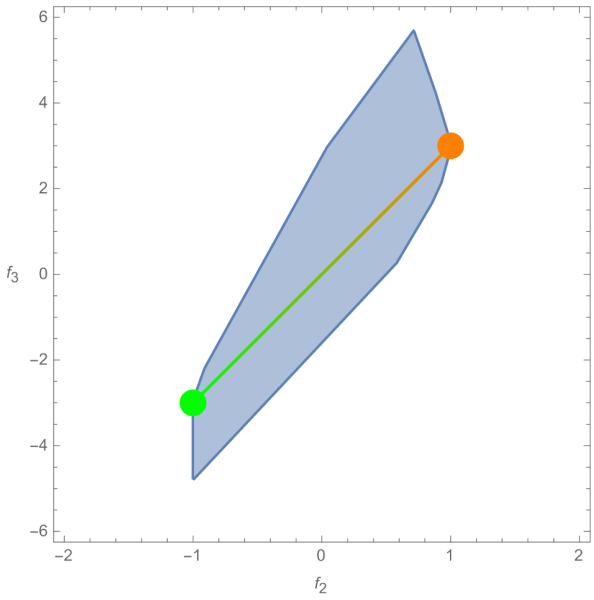

Figure 9. Causality bounds in the (f_2, f_3)-plane for $g_3 = 1$, $h_3 = 0$, $f_4 = f_2/2$, and $g_4 = 1$ which are consistent with the values of the scalar and axion partial UV completions. One can see that the points denoting the values of the partial UV completions, scalar in green and axion in orange, lie in the boundary of the causal region. The line connecting them corresponds to a partial UV completion involving both a scalar and an axion.

completions. This is done by allowing the remaining Wilson coefficients to depend on f_2, which will then once again act as a dialing parameter. One can extrapolate between both endpoints and obtain a full segment of partial UV completions as shown in figure 10. The segment is fully contained within our causality bounds, with the scalar and axion points exactly lying on the boundary, as was previously the case in the (f_2, f_3) and (f_2, g_3)-planes, respectively plotted in figures 9 and 6.

In this example, neither f_2 nor h_3 enjoy a sign-definite contribution to the time delay in either of the even and odd sectors. This way, the latter contributed respectively to left and right-sided bounds.

Bounds on f_3, g_3, and h_3. We now turn to analyze the bounds for the dimension-10 coefficients. For these parameters, we obtain bounds of the following form

$$f_3 + 3g_3 < X_{u_2^\ell} + Y_{u_2^\ell} h_3 \,, \tag{4.30}$$

$$-X_{u_4^\ell} - Y_{u_4^\ell} h_3 < f_3 - 3g_3 + 4h_3 < X_{u_4^\ell} + Y_{u_4^\ell} h_3 \,, \tag{4.31}$$

where $X_{u_{2,4}^\ell}$ depends on the other amplitude parameters as observed in figures 11, 12, and 13 as well as on the specific background. Thus, the value of $X_{u_4^\ell}$ and $Y_{u_4^\ell}$ can be different for the upper and lower bounds since it will be optimized to have the tightest bounds. This analysis simplifies in the even sector; for the choice of the amplitude parameters as in the axion partial UV completion, we get $X_{u_2^\ell} = 1/(\epsilon_1^2 \epsilon_2^2 \mathcal{B}^+)$ and in the odd sector for the scalar partial UV completion we have $X_{u_4^\ell} = 1/|\omega \Delta T^{(f_3)}_{b,4,\ell}(\omega)|$.

JHEP06(2024)146

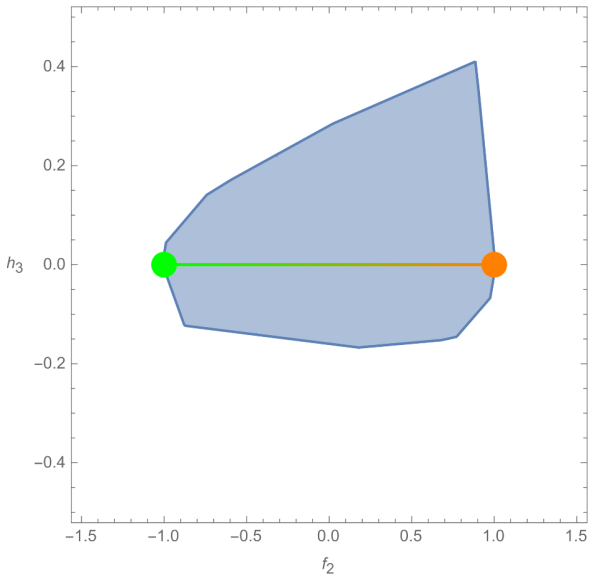

Figure 10. Causality bounds in the (f_2, h_3)-plane for $f_3 = 3f_2$, $g_3 = 1$, $f_4 = f_2/2$, and $g_4 = 1$ which are consistent with the values of the scalar and axion partial UV completions. The points denoting the values of the partial UV completions, scalar in green and axion in orange, lie in the boundary of the causal region as in the previous cases. Similarly, the line denoting the mixed partial UV completion of a scalar and axion also lies within the causal region.

On the $f_3 - g_3$ plane, we see that the even sector only gives rise to an upper bound due to the sign definite contribution from both g_3 and f_3. This upper bound becomes stronger as we increase h_3 since this can contribute with a negative time delay that needs to be balanced by a more positive contribution from f_3 and g_3. Meanwhile, the odd sector contributions are not sign definite and give both upper and lower bounds. The strength of these two-sided bounds does not change drastically when varying h_3 since the background is optimized so that the width of the bound on the f_3 direction is the smallest possible bound. While the strength of the bounds in the odd sector does not vary drastically with h_3, the location does change and moves towards the negative f_3 direction as h_3 is increased. Note that the values of h_3 considered here are chosen so that we have a non-vanishing causal region, which in these cases requires $h_3 \gtrsim 0$ as can be seen below.

In the $f_3 - h_3$ plane, we should expect upper and lower bounds. This is observed in figure 12 where the bounds arising from the even and odd sectors are plotted separately. We can appreciate that each sector separately does not give a compact region; it is the combination of both that gives rise to the compact causal region. On the even sector, the contribution of f_3 is sign definite, so we can only get an upper found, while in the odd sector, we have both an upper and lower bound. As in the $f_3 - g_3$ bounds, we have tight bounds on the odd sector for the scalar partial UV completion case since the contributions from all the other amplitude parameters vanish and the actual values of the UV completion lie on the boundary. Similarly, we observe that the axion partial UV completion is in the boundary of the even sector causal region. The bounds are not as strong as in the scalar completion case due to the sign-definite contribution of f_3. If we were to change the contributions from

JHEP06(2024)146

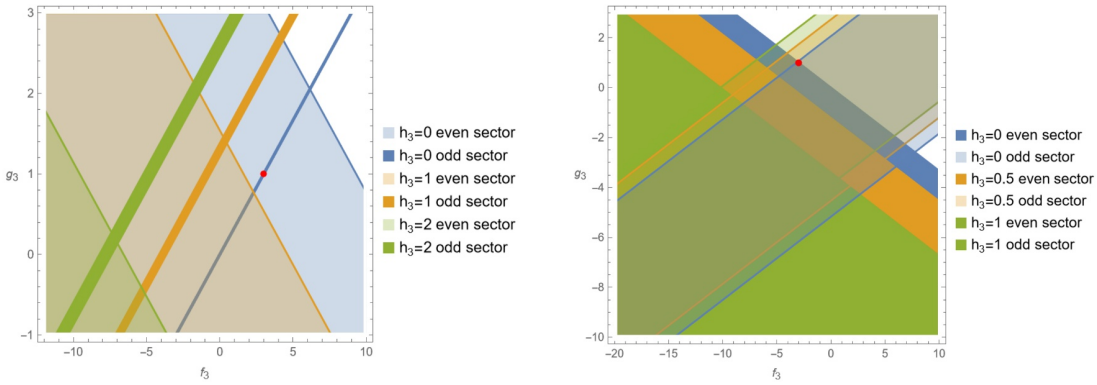

Figure 11. Causal bounds on $f_3 - g_3$ plane with varying h_3 for the odd and even sectors with the values of the other coefficients fixed as in the scalar partial UV completion on the left (with $(f_2, f_4, g_4) = (1, 1/2, 1)$) and the axion one on the right (with $(f_2, f_4, g_4) = (-1, -1/2, 1)$). The red dot indicates the value of the coefficients for the corresponding partial UV completion. The final causal region is obtained as the intersection of the causal regions for both the odd and even sectors. This region is not compact in the negative $f_3 - g_3$ direction. For clarity of the plots, we have chosen to depict the even sector as 'transparent' and the odd as 'solid' on the left plot corresponding the scalar UV completion while this is reverted on the right plot for the axion completion.

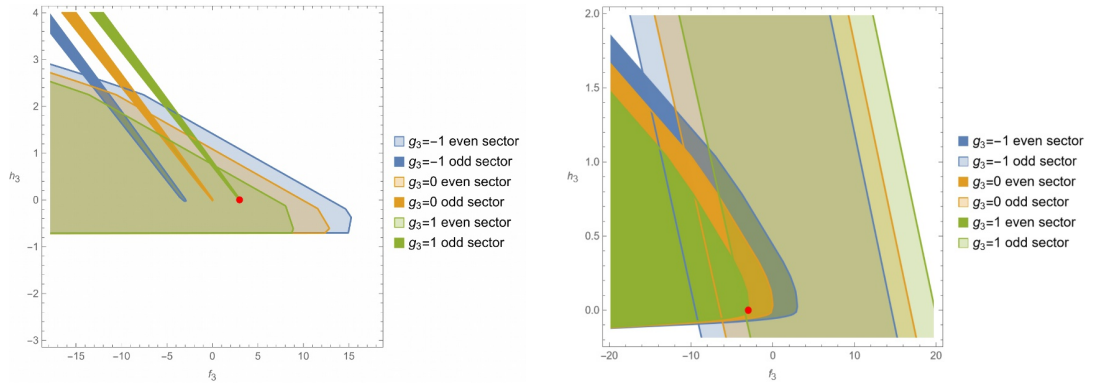

Figure 12. Causal bounds on $f_3 - h_3$ plane for the odd and even sectors with varying g_3 and all other parameters set by the values of the scalar (left) or axion (right) partial UV completions. More precisely, we have $(f_2, f_4, g_4) = (1, 1/2, 1)$ and $(-1, -1/2, 1)$ for the scalar and axion respectively. The final causal region is obtained as the intersection of the causal regions for both the odd and even sectors. The red dot represents the corresponding values of the partial UV completions and lies in the boundary of the causal region.

the dimension-12 coefficients, we would be able to tune the background to obtain a negative contribution to the odd sector time delay which leads to a stronger bound. The effect of this is to move the odd sector causal region further up so that it no longer intersects with the even sector causal region. This can be read as further constraints on the Wilsonian coefficients of the dimension-12 operators.

Last, we analyze the bounds on the $g_3 - h_3$ plane. The analysis above ($f_3 - h_3$ case) is identical for the $g_3 - h_3$ bounds since the contribution of g_3 is degenerate with the one in f_3. In the even sector, the f_3 and g_3 contributions have the same sign, but in the odd

JHEP06(2024)146

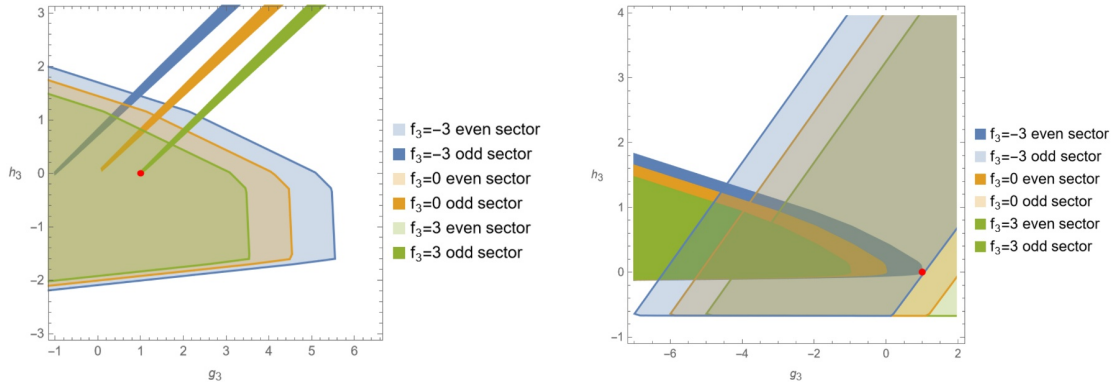

Figure 13. Causal bounds on $g_3 - h_3$ plane for the odd and even sectors with varying f_3 and all other parameters set by the values of the scalar (left) or axion (right) partial UV completions. Once again, we have $(f_2, f_4, g_4) = (1, 1/2, 1)$ and $(-1, -1/2, 1)$ for the scalar and axion respectively. As in the previous cases, the final causal region is obtained as the intersection of the causal regions for both the odd and even sectors and the red dot represents the corresponding partial UV completion.

sector, they have opposite signs, so the only difference will be the change in the sign of the slope of the odd sector bounds as seen in figure 13.

Bounds on f_4, g_4, and g_4'. The leading order contribution to the time delay from the dimension-12 operators is

$$\omega \Delta T_{b,\{2,4\},\ell} \supset 12(g_4 \pm 2f_4)\epsilon_1^2\epsilon_2^2\Omega^2\mathcal{C}^+\,, \tag{4.32}$$

where $\mathcal{C}^+ > 0$ is defined in eq. (4.20) and the $+(-)$ sign comes from the even (odd) sector. Thus, we expect to get bounds of the form:

$$g_4 + 2f_4 > Z_{u_2^\ell}\,, \quad g_4 - 2f_4 > Z_{u_4^\ell}\,, \tag{4.33}$$

where $Z_{u_{2,4}^\ell}$ are numbers determined by the optimization of the background which also depend on the other scattering amplitude parameters. They depend very weakly on f_2 and only become slightly tighter as we approach $f_2 = \pm 1$ boundaries. Together this give rise to a lower bound $g_4 > (Z_{u_2^\ell} + Z_{u_4^\ell})/2$ as predicted in table 2. By optimizing our bounds, we are able to find

$$g_4 > 0\,, \tag{4.34}$$

this lower bound can be stronger for specific f_3, g_3, h_3 values.

In figure 14, we observe the bounds on the $f_4 - g_4$ plane. The lower bound on f_4 becomes stronger when $f_3 + 3g_3 > 0$ since these terms can give a negative contribution to the time delay of u_2^ℓ which in turn requires a larger positive value of f_4 to not obtain an observable time advance. Meanwhile, a non-zero $f_3 - 3g_3$ contribution can be tuned to give a negative time delay for u_2^ℓ so that the upper bound on f_4 becomes stronger. Both the lower and upper bounds on f_4 are improved for a non-zero h_3. This is a large effect compared to that of f_3 and g_3 since these parameters have a suppression of B^2/R^2 in the integrand of the time delay with respect to a part of the h_3 contribution, (see table 2). In the odd sector, the non-suppressed

JHEP06(2024)146

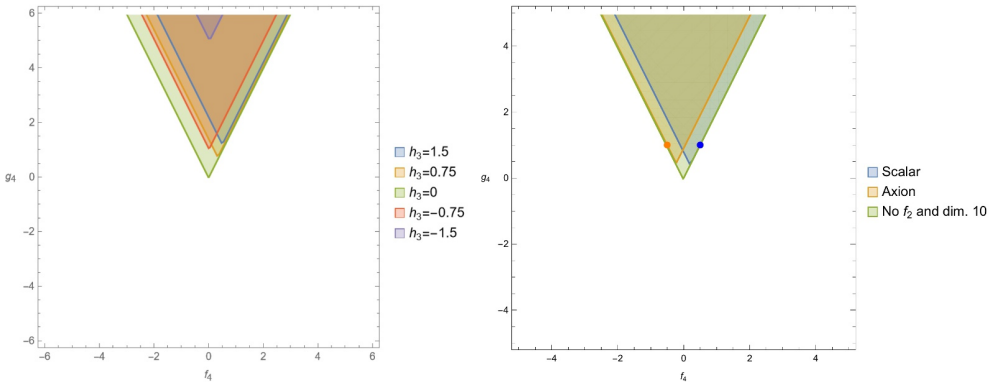

Figure 14. Bound on the $f_4 - g_4$ plane. The left-hand side has $f_2 = f_3 = g_3 = 0$ and varying h_3. On the right-hand side, we choose the parameters not being plotted to have the corresponding values of the partial UV completion as in table 1. The scalar (blue) has $(f_2, f_3, g_3, h_3) = (1, 3, 1, 0)$, the axion (orange) $(f_2, f_3, g_3, h_3) = (-1, -3, 1, 0)$, and the green region $f_2 = f_3 = g_3 = h_3 = 0$. Note that in principle, the plots extend infinitely to the top since we cannot bound g_4 from above; however, the EFT makes sense at the cutoff Λ only if all Wilsonian coefficients are taken to at most roughly of order 1.

h_3 contribution is positive definite so a positive h_3 does not improve largely the upper bounds on f_4. This is not the case in the even sector so a positive h_3 does improve significantly the lower bounds. For a negative h_3 the non-suppressed contributions from both the even and odd sectors can be made negative and largely improve both upper and lower bounds.

Note that up to the EFT order we are working on, we have no contribution from the Wilson coefficient c_7, or equivalently from the scattering amplitude parameter g_4'. The contribution of g_4' (c_7) starts at order $\epsilon_1^2\epsilon_2^4$. If we choose to include this contribution, but still neglect all the WKB corrections (since they are not calculable in our setting), it would require that we neglected $\epsilon_1^2\epsilon_2^2/\Omega^2$ corrections, but include $\epsilon_1^2\epsilon_2^4$, $\epsilon_1^2\epsilon_2^4\Omega^2$, $\epsilon_1^2\epsilon_2^6\Omega^2$ terms. The latter contributions arise from operators with dimension-14 and 16. In this new setting, the validity of the EFT will require a large Ω bounded as $\epsilon_2^{-1} \ll \Omega \ll \epsilon_2^2$ which will naturally enhance the new contributions from the operators of dimension-14 and 16. While we can tune the background solution to decrease the effect of these operators and enhance that of g_4', these explorations are beyond the scope of this work. Instead, we can parameterise the amplitude as in [75, 76], in which case we can obtain bounds for both $g_{4,1}$ and $g_{4,2}$ parameters defined in table 4. This simply follows from their leading order contribution to the time delay which will give bounds of the form

$$2f_4 + g_{4,1} + 2g_{4,2} > A_{u_2^\ell}\,, \quad -2f_4 + g_{4,1} + 2g_{4,2} > A_{u_4^\ell}\,. \tag{4.35}$$

4.2.2 Case $g_2 = 0$

One can show that when $g_2 = 0$ causal propagation implies[8]

$$f_2 = f_3 = g_3 = h_3 = 0\,. \tag{4.36}$$

[8]Strictly speaking we obtain bounds of the form $-\epsilon < \mathcal{W}_J < \epsilon$, where ϵ is smaller than the WKB and EFT contributions that we are neglecting so we can effectively take $\epsilon = 0$.

JHEP06(2024)146

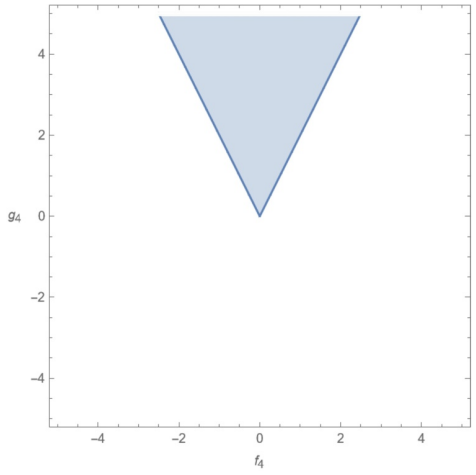

Figure 15. Bound on the $f_4 - g_4$ plane for the case $g_2 = 0$. These bounds are independent on the value of all the other scattering amplitude parameters.

Once both f_2 and g_2 vanish, the requirements for the validity of the EFT in eq. (4.12) change. Instead, we have a less restrictive situation where:

$$\epsilon_1, \epsilon_2 \ll 1\,, \quad \epsilon_2^{1/2} \ll \Omega \ll \frac{1}{\epsilon_2}\,. \tag{4.37}$$

Using this new setup, we can find the causal bounds on the $f_4 - g_4$ plane as shown in figure 15. We can see that the bounds are equal to the $g_2 \neq 0$ case with all other amplitude parameters set to zero, that is, they are given by

$$2f_4 + g_4 > 0\,, \quad -2f_4 + g_4 > 0\,, \tag{4.38}$$

which implies that g_4 is positive. Note that since we can only obtain a one-sided bound for the g_4 coefficient within our EFT setup, we are only able to constrain its sign. One should note that f_4 will be required to vanish if g_4 were to vanish.

5 Positivity and causality

After deriving the causality and positivity bounds for the low-energy parameter space of the massless photons EFT in eq. (2.3), we proceed to compare these results and discuss their complementary. In all of the plots in this section, the regions constrained by IR causality and positivity will be bounded by a thick line and a dashed line respectively. Recall that in this (and previous sections) we have set $g_2 = 1$. We proceed to compare the strength of causality and positivity bounds for different slicings of the parameter space showing the cases where positivity bounds can give stronger results than causality in section 5.1 and the cases where positivity and causality complement each other in section 5.2. Finally, we comment on the case $g_2 = 0$ in section 5.3.

It is worth highlighting that given the set of assumptions that we make in deriving either the IR causality bounds or the positivity bounds (summarized in table 3), we do not claim to possess the absolute most restrictive bounds that could possibly arise from said assumptions.

JHEP06(2024)146

Property	Causality Bounds	Positivity Bounds
Lorentz invariance	• Lorentz invariant EFT	• Invariant EFT and UV completion • Crossing symmetry
Unitarity	• Hermitian Hamiltonian: real Wilson coefficients	• Positive discontinuity of the EFT and UV amplitude
Causality	• No resolvable time advance	• Analyticity of amplitude in the complex s plane for fixed t
Locality	• IR theory is local	• IR and UV theories are local • Froissart-like bound in the UV
Other assumptions	• EFT and WKB expansions under control • Background generated by localized external source	• IR EFT is under perturbative control

Table 3. Summary of the assumptions underlying the positivity and causality bounds.

In particular, this means that where regions allowed by causality and positivity do not overlap, it does not imply that somehow the two approaches are in contradiction. For example, if a region of parameter space is allowed by current positivity bounds but excluded by the causality bounds we have derived, this would not imply that the assumptions on the positivity side allow for causality-violating parameter values nor that there is any contradiction. Rather it would simply indicate that at the current level, the analytic positivity bounds we have derived are not the most optimal nor the most restrictive constraints and signal that pushing further positivity bounds beyond the current state-of-the-art one would likely be able to prove that this region of parameter space is no longer allowed by positivity. When this occurs, this should be read as a way to read from causality how one would expect future positivity bounds to evolve as they become more restrictive.

5.1 Positivity bounds are stronger then causality

Bounds on f_4 and g_4. Unlike positivity bounds, causality constraints cannot provide compact bounds on all the parameter space in EFT for fixed g_2. As mentioned previously, due to technicalities of the WKB approximation, there is no upper bound on g_4 from causality, see figure 16(a). Positivity bounds provide the upper limit on $g_4 < g_2$. The form of the allowed region depends on the value of f_2, shrinking to a single line for the extreme values $f_2 = \pm 1$. The parameter range allowed by causality is much larger in this case. Remarkably, its form resembles the same cone as obtained from positivity.

Bounds for $g_4 = 0$. The non-linear bounds in (3.33), (3.38) only allow for null values of $g_3,\ f_3,\ h_3$. The causality constraints are weaker in this case, still allowing for certain ranges expanding with g_3, as it is shown in figure 16(b). The coefficient g_3 is bounded only from above, and f_3, h_3 are in the compact ranges which grow when g_3 is decreasing.

Bounds on (f_2, f_3) and (f_2, h_3) planes. In both the (f_2, f_3) and (f_2, h_3) planes the positivity bounds exactly reduce to the line interpolating between the scalar and axion UV completions as seen in figure 17. In these cases, the positivity bounds coincide with a

JHEP06(2024)146

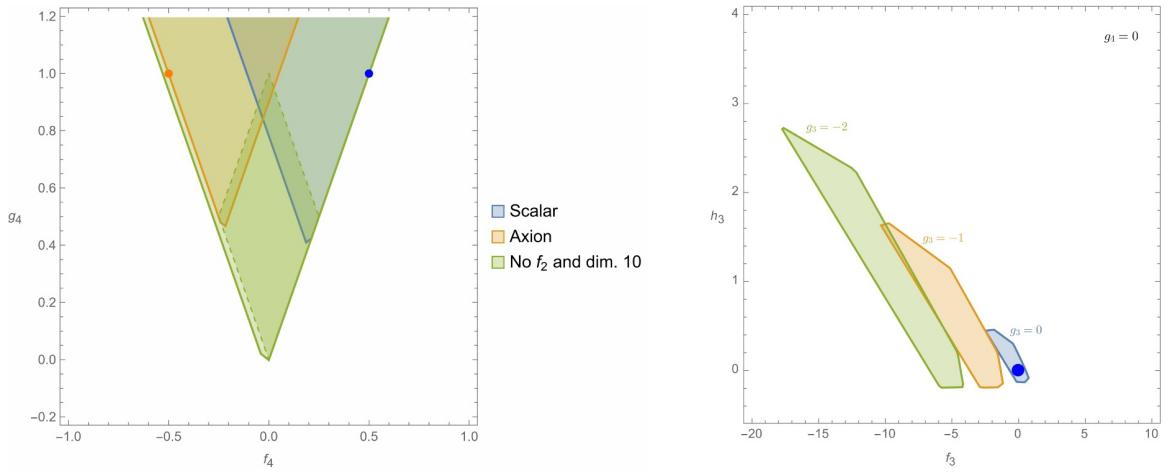

(a) (b)

Figure 16. (a) Causality (solid) and positivity (dashed) bounds for g_4–f_4. The green region corresponds to $(f_2, f_3, g_3, h_3) = (0, 0, 0, 0)$, the blue to $(1, 3, 1, 0)$ (values taken by the scalar UV completion) and the orange to $(-1, -3, 1, 0)$ (values taken by the axion UV completion). The blue and orange points are correspond to values of (f_4, g_4) produced by the scalar and axion UV completions respectively. (b) f_3–h_3 plane for varying $g_3 = 0, -1, -2$ and all other coefficients zero. Positivity bounds leave $g_3 = h_3 = f_3 = 0$ as the only possibility in this case. The causality bounds are compact in f_3 and h_3 for any given g_3 but generically, the direction $f_3 + 3g_3$ is not bounded from below, see eq. (4.30).

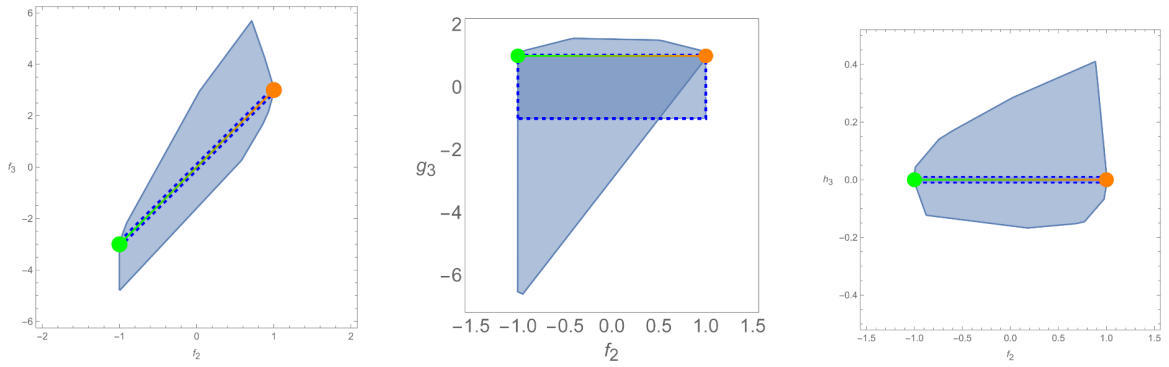

(a) (b) (c)

Figure 17. We plot the causality (thick line) and positivity (dashed line) bounds for different slicings of our parameter space and set the parameters not being plotted to values consistent with the scalar and axion partial UV completions. The slices we plot are: (a)(f_2, f_3)-plane for $g_3 = 1$, $h_3 = 0$, $f_4 = f_2/2$, and $g_4 = 1$; (b) (f_2, g_3) plane for $f_3 = 3f_2$, $h_3 = 0$, $f_4 = f_2/2$, and $g_4 = 1$; (c) (f_2, h_3) plane for $f_3 = 3f_2$, $g_3 = 1$, $f_4 = f_2/2$, and $g_4 = 1$. One can see that the points denoting the values of the partial UV completions, scalar in green and axion in orange, lie in the boundary of the causal region. The line connecting them corresponds to a partial UV completion involving both a scalar and an axion.

JHEP06(2024)146

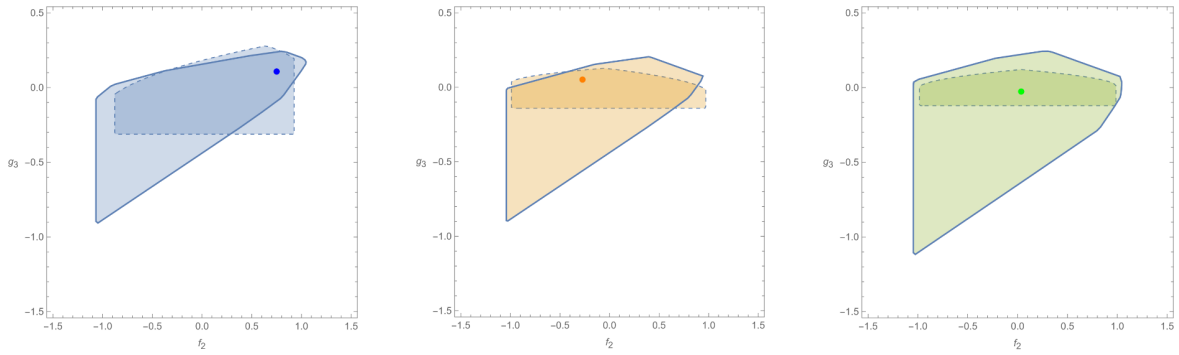

(a) Scalar (b) Spinor (c) Vector

Figure 18. Causality (thick line) and positivity (dashed line) bounds in the (f_2, g_3) plane for various values of (f_3, h_3, f_4, g_4) that are consistent with the scalar, spinor and vector QED partial UV completions, namely $(f_3, h_3, f_4, g_4) \sim (0.36, 0.04, 0.01, 0.10)$ for the scalar, $(-0.13, -0.01, 0.00, 0.02)$ for the spinor and $(0.02, 0.00, 0.00, 0.01)$ for the vector. The exact values are given in table 1.

one-dimensional region of the parameter space that admits a partial UV completion and are thus stronger than the causality bounds, which give an allowed area surrounding the UV completion segment.

5.2 Complementarity of the positivity and causality bounds

We present here several slices showing that causality bounds, being more sensitive to the different combinations of the EFT parameters, can give additional constraints compared to the known positivity bounds. Typically, the positivity constraints on f_3 and h_3 are relatively weak, see figure 3.

Bounds on f_2 and g_3. In the (f_2, g_3) plane we see that both partial UV completions and the line joining them lie within the region allowed by causality and positivity bounds. The positivity bounds, denoted by the dashed boundary, are more constraining overall but allow for parameter values that are forbidden by causality bounds. Here we see for the first time that causality bounds provide additional information on the parameter space than that obtained by positivity alone. Once again we clarify that this does not mean that theories satisfying positivity bounds are not causal, it just shows that these bounds can probe different regions of the parameter space.

Around QED UV completions. Turning now to the loop level QED partial UV completions, the causality bounds are compared to the region compatible with positivity in figure 18. While positivity bounds give a smaller allowed region than causality bounds, we see that they actually probe different regions for the scalar and spinor QED cases. Thus, combining both bounds will ultimately reduce the allowed region. Note finally that all QED partial UV completions lie within both causality and positivity bounds, as expected for consistency.

Bounds on f_3, g_3, and h_3. Let us start by discussing the (f_3, g_3) plane where all other coefficients are set to the values of either the scalar or axion UV completions found in table 1. The bounds are reported in figure 19. The first thing to note is that even though allowed

JHEP06(2024)146

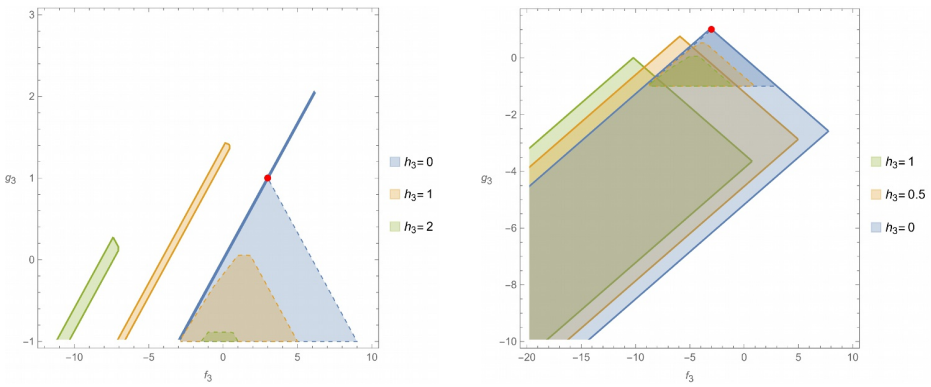

Figure 19. Causality (thick line) and positivity (dashed line) bounds on (f_3, g_3) plane with varying h_3 and the values of the other coefficients fixed as in the scalar partial UV completion on the left and the axion one on the right. In particular, the left panel has $(f_2, f_4, g_4) = (1, 1/2, 1)$ and the right one $(f_2, f_4, g_4) = (-1, -1/2, 1)$.

regions exist both from causality and positivity bounds for $h_3 = 1$ and 2, their union is empty and hence these values are discarded in the sense that they cannot correspond to theories endowed with causal propagation in both the IR and UV. The more interesting case, $h_3 = 0$, corresponding to the scalar or axion partial UV completions is allowed by both methods. For the left-hand side (scalar UV completion parameters), the causality bounds are much more constraining than their positivity counterparts in the $f_3 - 3g_3$ direction. As explained previously, this is due to having the additional parameter fixed as in the scalar UV completion which implies that they do not contribute to the time delay in the odd sector. On the other hand, positivity bounds provide a slightly lower upper value than causality in the $f_3 + 3g_3$ direction and also a lower bound that we cannot obtain from causality.

For the right side of figure 19, we see that the axion partial UV completion is consistent with both methods as expected. This time, the positivity bounds are stronger than the bounds obtained from IR causality but it is still interesting to compare them since, for instance, their union becomes smaller as h_3 is raised. Thus, utilizing both bounds allows us to rule out theories with values of h_3 further away from the axion UV completion value, $h_3 = 0$.

Let us now analyze the (f_3, h_3) plane, where the values of all other parameters are consistent with the scalar partial UV completion (left panel of figure 20). One can see that the causality bounds are much more constraining than their positivity counterparts, except in the case $g_3 = 1$ where the latter reduce to the single scalar UV completion point. For the other cases, even though both sets of bounds have a finite size, their union also reduces to a single point,[9] once again proving the power of this combined approach. Turning now to the right panel (axion UV completion parameters), both causality and positivity bounds have similar strength, with the causality ones being slightly more constraining this time. The scalar and axion UV partial UV completions are consistent with both methods and lie in the boundary of the bounds.

The (g_3, h_3) case is very interesting. When focusing on the value $f_3 = 3$ on the left panel of figure 21, which is precisely the value that is compatible with the scalar partial UV completion,

[9]Note that this statement holds even if we choose a different order one number for the causality conditions as analyzed in figure 6.

JHEP06(2024)146

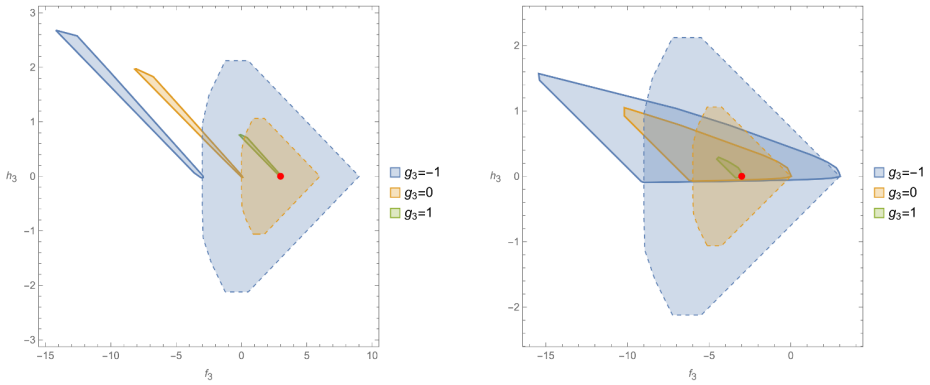

Figure 20. Causality (thick line) and positivity (dashed line) bounds on (f_3, h_3) plane with varying g_3 and all other parameters set by the values of the scalar (left) or axion (right) partial UV completions. In particular, the left panel has $(f_2, f_4, g_4) = (1, 1/2, 1)$ and the right one $(f_2, f_4, g_4) = (-1, -1/2, 1)$.

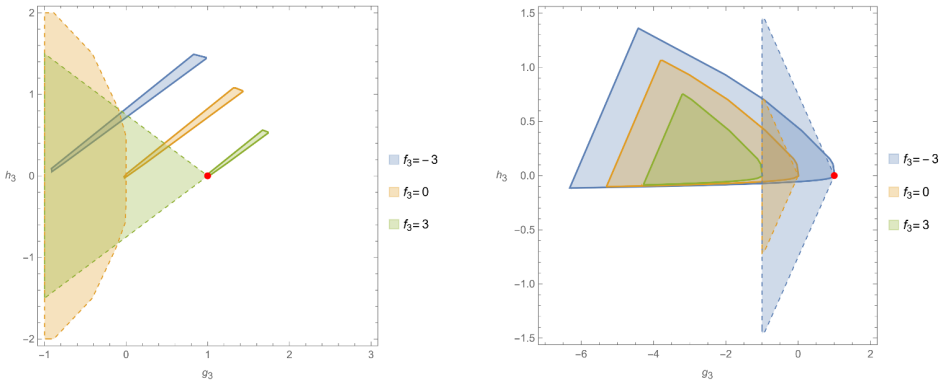

Figure 21. Causality (thick line) and positivity (dashed line) bounds on (g_3, h_3) plane with varying f_3 and all other parameters set by the values of the scalar (left) or axion (right) partial UV completions. In particular, the left panel has $(f_2, f_4, g_4) = (1, 1/2, 1)$ and the right one $(f_2, f_4, g_4) = (-1, -1/2, 1)$.

the intersection of the causality and positivity bounds reduce to this single point. This example perfectly illustrates the power of combining the two methods, which can dramatically reduce the space of causal theories, to the point of converging to a point-like region.

The right panel shows the axion case. The causality bounds are slightly less constraining than the positivity ones but their union is smaller. It is worth noting that the axion partial UV completion is consistent with both bounds. If $f_3 = 3$ (with all other coefficients set to the axion completion values) then positivity bounds shrink the allowed region to a single point allowing only for $(g_3, h_3) = (0, -1)$, which is also consistent with causality.

So far we were looking at extreme parameter choices close to the values of either scalar or axion UV completions. We know that these values are at the boundary of the 6-dimensional allowed region. To visualize what happens inside the constrained volume, instead of in a slice, we present the 3D plots for $h_3 - g_3 - f_3$ parameters when $f_2 = f_4 = 0$ which illustrate the complementarity of the positivity and causality bounds, see figure 22. It is interesting to observe from these plots that causality can constrain h_3 direction stronger than positivity, especially for the lower bound on h_3.

JHEP06(2024)146

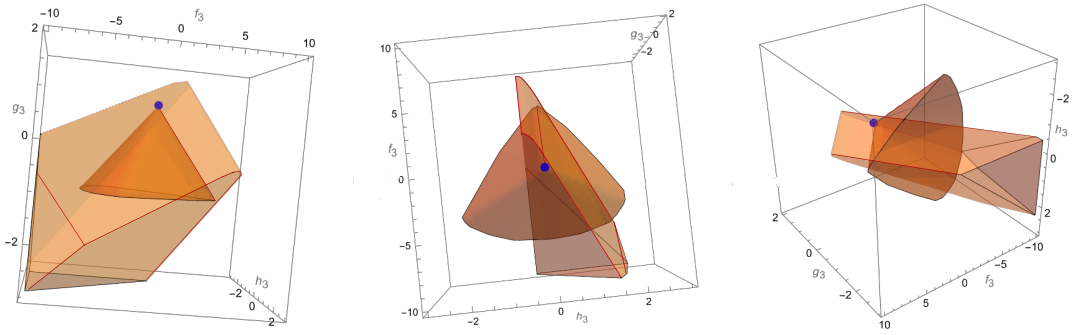

Figure 22. 3-dimensional plot of positivity and causality bounds on g_3, h_3, f_3 for $f_2 = f_4 = 0$, $g_4 = 1$ seen from different directions. Positivity bounds are shown in a solid colour while the causality constraint is plotted with a transparent lighter colour. The blue point corresponds to a partial UV completion with an axion and scalar with the same coupling strength.

5.3 Case $g_2 = 0$

As it was discussed in section 3, positivity bounds do not allow to have $g_2 = 0$ in an interacting theory. In particular, the non-linear bounds in (3.37) force all the EFT coefficients that we considered to be zero when $g_2 = 0$. On the other hand, causality bounds are independent of any assumptions about the UV theory and allow us to probe low-energy properties. On the contrary, causality bounds still allow an interacting theory with $g_2 = 0$. More precisely, the causality requirements lead to $f_2 = f_3 = g_3 = h_3 = 0$. However, causality conditions imply only $g_4 > 0$ and $-g_4/2 < f_4 < g_4/2$, see figure 15. We can see that this is consistent with having all scattering amplitude parameters vanishing in the free theory as in the results obtained from positivity bounds. In our current setting, we cannot obtain an upper bound on g_4 since the non-sign definite contributions cannot be included consistently up to the order in the WKB expansion that we can compute. If we were able to find a consistent setting to include these corrections, we would obtain an upper bound on g_4 that very likely will impose $g_4 = 0$ and hence $f_4 = 0$.

6 Conclusions

In this work, we have derived two sets of consistency conditions on the photon EFT parameters (defined in (2.3)) based on different assumptions, namely, positivity bounds and causality constraints. The latter are obtained by requiring the absence of a resolvable time advance for photon modes propagation on top of a non-trivial background generated by an external source. Meanwhile, the positivity bounds are based on analytic properties of the scattering amplitudes, which can be inferred by assuming microcausality. However, they have additional requirements on the UV completion, such as a Froissart-like bound. The assumptions of each method are summarized in table 3. Note that, while positivity bounds require the assumption of unitarity, they do not use its full power. Thus, the bounds on the Wilson coefficients could be improved by imposing full non-linear unitarity with numerical techniques. The upshot of our work is that we do not need to use numerical techniques to obtain strong constraints on the Wilson coefficients. Instead, we can combine different analytic methods (positivity and causality bounds) to obtain strong constraints. It is also worth noting that as a consistency

JHEP06(2024)146

check, we have verified that known, healthy, partial UV completions lie within the allowed region of both positivity and causality bounds.

Interestingly, we have shown that applying strict positivity of the time delay would rule out known (partial) UV completions. In other words, known consistent (partial) UV completion lead to a negative contribution to the time delay which is unresolvable and hence consistent with our notion of causality but would be misidentified if the appropriate resolvability condition had not been properly accounted for.

When comparing the positivity and causality bounds obtained in this paper, we found that in certain regions of the parameter space positivity leads to stronger bounds, but in other regions causality and positivity are complementary. When we refer to complementarity, we refer to the comparison between our causality bounds and our analytic positivity bounds and not numerically optimized positivity bounds or those using the full power of unitarity. We found that the causality bounds derived here are predominantly double-sided and compact, with a few exceptions, especially the g_4 case that does not admit any upper bound in our current setup. On the other hand, positivity bounds always lead to compact regions. Nevertheless, there are other cases where our bounds are complementary and their combination can lead to a great reduction of the allowed parameter space as seen in 5.2. An interesting case worth highlighting is the bound on h_3. The positivity bounds are symmetric with respect to $h_3 \to -h_3$, but the causality bounds are not. From the causality point of view, the time delay of the odd modes has a large positive h_3 contribution which generically implies a strong lower bound on h_3, but not so strong upper bound. Thus, causality can improve the lower bound on h_3 obtained from our analytic positivity bounds.

In some slices of the parameter space, we have found that the positivity and causality allowed regions are disjoint, thus those parameters are ruled out. We highlight that this does not imply that a theory satisfying positivity bounds is acausal in the IR. Both our causality and positivity bounds do not exhaust the full power of the assumptions used to derive them. These extreme examples simply show that our bounds probe different regions of the parameter space and that combining them can be extremely powerful. It would be interesting to combine all the existing constraints on photon EFTs from previous works such as [75–77] together with the present bounds to find even stronger bounds on the EFT Wilson coefficients. Similarly, it is worth noting that causality bounds can be applied to general theories involving operators with higher-point interactions. Thus, while positivity bounds mostly focus on $2-2$ scattering, causality can also be complementary to these explorations by constraining higher-point interactions. Generically, combining different techniques to bound EFT parameters can be very fruitful and the full power of combining causality and positivity bounds is yet to be proved.

Acknowledgments

We would like to thank Calvin Chen, Greg Kaplanek, Aoibheann Margalit and Andrew J. Tolley for useful discussions. The work of MCG, AT and CdR at Imperial is supported by STFC grant ST/T000791/1. VP is funded by the Imperial College President's Fellowship. SJ is supported by an STFC studentship. CdR is also supported by a Simons Investigator award 690508. The work of AT at final stage is supported in part by the National Natural Science Foundation of China (NSFC) under Grant No. 12147103.

JHEP06(2024)146

A Equations of motion

The equation of motion for the vector field A^μ with Lagrangian given by eq. (2.3) and sourced by an arbitrary current J^ν is

$$\partial^\mu \mathcal{E}^{(F)}_{\mu\nu} = g J_\nu \,, \tag{A.1}$$

where

$$\begin{aligned}
\mathcal{E}^{(F)}_{\mu\nu} \equiv\, & F_{\mu\nu} - 8\frac{c_1}{\Lambda^4} F_{\mu\nu} F^{\alpha\beta} F_{\alpha\beta} - 8\frac{c_2}{\Lambda^4} F_{\mu\alpha} F_{\nu\beta} F^{\alpha\beta} \\
& + 2\frac{c_3}{\Lambda^6}\Big[F_\mu{}^\alpha \Big(\partial_\alpha F_\nu{}^\beta \partial_\gamma F_\beta{}^\gamma + F^{\beta\gamma} \partial_\gamma \partial_\alpha F_{\nu\beta} \Big) - F^{\alpha\beta} \partial_\alpha F_\mu{}^\gamma (\partial_\gamma F_{\nu\beta} + \partial_\nu F_{\beta\gamma}) \Big] - (\mu \leftrightarrow \nu) \\
& + \frac{c_4}{\Lambda^6}\Big[\frac{1}{2} F_\mu{}^\alpha F_\nu{}^\beta \Big(\partial_\gamma \partial_\beta F_\alpha{}^\gamma - \partial_\gamma \partial_\alpha F_\beta{}^\gamma \Big) - F_\mu{}^\alpha \Big((\partial_\alpha F_{\beta\gamma} - \partial_\beta F_{\alpha\gamma}) \partial^\gamma F_\nu{}^\beta + \partial_\gamma F_\beta{}^\gamma \partial_\nu F_\alpha{}^\beta \\
& \qquad + F^{\beta\gamma} \partial_\nu \partial_\gamma F_{\alpha\beta} \Big) - F^{\alpha\beta} \Big(\partial^\gamma F_{\mu\alpha} (\partial_\beta F_{\nu\gamma} - \partial_\nu F_{\beta\gamma}) + \partial_\alpha F_\mu{}^\gamma \partial_\nu F_{\beta\gamma} \Big) \Big] - (\mu \leftrightarrow \nu) \\
& + \frac{c_5}{\Lambda^6}\Big[F_\mu{}^\alpha \Big(\partial_\alpha F_{\beta\gamma} \partial_\nu F^{\beta\gamma} + F^{\beta\gamma} \partial_\nu \partial_\alpha F_{\beta\gamma} \Big) + F^{\alpha\beta} \Big(\partial_\gamma F_{\alpha\beta} \partial_\mu F_\nu{}^\gamma + \partial_\gamma F_\mu{}^\gamma \partial_\nu F_{\alpha\beta} \Big) \\
& \qquad + F_{\mu\nu} \Big(F^{\alpha\beta} \partial_\gamma \partial_\beta F_\alpha{}^\gamma + \partial_\beta F_{\alpha\gamma} \partial^\gamma F^{\alpha\beta} \Big) \Big] - (\mu \leftrightarrow \nu) \\
& + \frac{1}{2}\frac{c_6}{\Lambda^8}\Big[-F_\mu{}^\alpha \partial_\nu \partial_\alpha \Big(\partial_\rho F_{\beta\gamma} \partial^\rho F^{\beta\gamma} \Big) - \partial_\mu F_\nu{}^\alpha \partial_\alpha \Big(\partial_\rho F_{\beta\gamma} \partial^\rho F^{\beta\gamma} \Big) - \partial_\alpha F_\mu{}^\alpha \partial_\nu \Big(\partial_\rho F_{\beta\gamma} \partial^\rho F^{\beta\gamma} \Big) \\
& \qquad + 2\partial^\alpha F_{\mu\nu} \Big(2\partial^\rho F^{\beta\gamma} \partial_\gamma \partial_\alpha F_{\beta\rho} + \partial_\alpha F^{\beta\gamma} \partial_\gamma \partial^\rho F_{\beta\rho} + F^{\beta\gamma} \partial_\alpha \partial_\gamma \partial^\rho F_{\beta\rho} \Big) \\
& \qquad + 4\Box F_{\mu\nu} \partial_\beta \Big(F_{\alpha\gamma} \partial^\gamma F^{\alpha\beta} \Big) \Big] - (\mu \leftrightarrow \nu) \\
& + \frac{c_7}{\Lambda^8}\Big[\partial_\mu F^{\alpha\beta} (\partial_\gamma F^{\gamma\rho} \partial_\nu \partial_\rho F_{\alpha\beta} - \partial_\alpha F^{\gamma\rho} \partial_\nu \partial_\beta F_{\gamma\rho}) + \partial^\alpha F_{\mu\nu} \partial^\rho \Big(\partial_\beta F^{\beta\gamma} \partial_\gamma F_{\alpha\rho} \Big) \\
& \qquad + 2\partial_\alpha \partial_\gamma F_{\mu\nu} \partial_\rho \Big(F^{\alpha\beta} \partial_\beta F^{\gamma\rho} \Big) + F^{\alpha\beta} \partial_\mu \partial_\alpha F^{\gamma\rho} \partial_\nu \partial_\beta F_{\gamma\rho} \Big] - (\mu \leftrightarrow \nu) \\
& + \frac{c_9}{\Lambda^8}\Big[-F_{\mu\alpha} \partial_\gamma \partial^\rho \Big(\partial^\alpha F_{\beta\rho} \partial_\nu F^{\beta\gamma} \Big) + 2\partial_\mu F^{\alpha\beta} \partial^\rho F_{\alpha\gamma} \partial^\gamma \partial_\beta F_{\nu\rho} + 2F^{\alpha\beta} \partial_\mu \partial^\gamma F_{\beta\rho} \partial^\rho \partial_\alpha F_{\nu\gamma} \\
& \qquad + \partial_\beta F_{\mu\alpha} \partial^\rho \Big(\partial^\alpha F_{\gamma\rho} \partial_\nu F^{\beta\gamma} + \partial^\alpha F^{\beta\gamma} \partial_\nu F_{\gamma\rho} - F_{\gamma\rho} \partial^\alpha \partial_\nu F^{\beta\gamma} - F^{\beta\gamma} \partial^\alpha \partial_\nu F_{\gamma\rho} \Big) \Big] - (\mu \leftrightarrow \nu) .
\end{aligned} \tag{A.2}$$

In section 4.1, we focus on the perturbations around a spherically symmetric background by perturbing the field as in eq. (4.2). In this setting, one can find that one of Maxwell's equations lead to a constraint and fixes one of the unphysical modes. To find this constraint, we perform a field-redefinition of u_1^ℓ and write

$$\begin{aligned}
v_1^\ell \equiv\, & \frac{i\omega u_1^\ell}{r} - \Big(u_2^\ell \Big)' - \frac{16}{\Lambda^4}(2c_1 + c_2) A_0' A_0'' u_2^\ell \\
& - \frac{2}{\Lambda^6}\frac{1}{r}\Big\{ c_3 A_0' (A_0' + 4r A_0'') \Big(u_2^\ell \Big)'' + 2c_3 \Big(2r (A_0'')^2 + A_0' \Big(3A_0'' + 2r A_0^{(3)} \Big) \Big) \Big(u_2^\ell \Big)' \\
& + \Big[c_3 \Big(\omega^2 - \frac{2}{r^2} \Big) (A_0')^2 + A_0'' \Big\{ 2(3c_3 - c_4 - 2c_5) A_0'' + 3(c_3 - c_4 - 2c_5) r A_0^{(3)} \Big\} \\
& + \frac{A_0'}{r} \Big\{ 2\Big(2c_3 (r^2\omega^2 - 1) + c_4 + 2c_5 \Big) A_0'' + 2(3c_3 - c_4 - 2c_5) r A_0^{(3)} + (c_3 - c_4 - 2c_5) r^2 A_0^{(4)} \Big\} \Big] \Big\} u_2^\ell \\
& + \frac{1}{\Lambda^8} \sum_{n=0}^{4} d_n (u_2^\ell)^{(n)} \,,
\end{aligned} \tag{A.3}$$

JHEP06(2024)146

where

$$
\begin{aligned}
d_0 = {} & 8\Big(-c_8\Big(L^2-3\Big)+2c_6+c_7\Big)\frac{(A_0')^2}{r^5}+4\Big((3c_6+c_8)L^2-11c_6-4c_7-9c_8\Big)\frac{A_0'A_0''}{r^4} \\
& +\Big((2c_6+c_8)L^2+2c_7+10c_8\Big)\frac{\omega^2(A_0')^2}{r^3}+4(7c_6+3c_7+2c_8)\frac{A_0'A_0^{(3)}}{r^3}+4(7c_6+2c_7+3c_8)\frac{(A_0'')^2}{r^3} \\
& +\Big(-c_8\Big(L^2+12\Big)-16c_6-20c_7\Big)\frac{\omega^2A_0'A_0''}{r^2}-2\Big(c_6\Big(L^2+3\Big)+2c_7-c_8\Big)\frac{A_0'A_0^{(4)}}{r^2} \\
& -2\Big(c_6\Big(3L^2+7\Big)+6c_7-c_8\Big)\frac{A_0''A_0^{(3)}}{r^2}-(2c_6+c_8)\frac{\omega^4(A_0')^2}{r} \\
& +2(-c_6+7c_7+5c_8)\frac{\omega^2A_0'A_0^{(3)}}{r}+2(9c_7+5c_8)\frac{\omega^2(A_0'')^2}{r} \\
& -2\left((c_6+c_8)\frac{A_0'A_0^{(5)}}{r}+2(3c_6-c_7+2c_8)\frac{A_0''A_0^{(4)}}{r}+(5c_6-2c_7+3c_8)\frac{(A_0^{(3)})^2}{r}\right) \\
& +c_8\omega^4A_0'A_0''+\omega^2\Big((2c_6+8c_7+5c_8)A_0^{(4)}A_0'+2(3c_6+8c_7+4c_8)A_0^{(3)}A_0''\Big) \\
& -2(c_6+c_8)\Big(A_0''A_0^{(5)}+3A_0^{(3)}A_0^{(4)}\Big)+128(2c_1+c_2)^2(A_0')^3A_0'',
\end{aligned}
\tag{A.4}
$$

$$
\begin{aligned}
d_1 = {} & 4\Big(c_7-c_8\Big(L^2+2\Big)\Big)\frac{(A_0')^2}{r^4}+4\Big(c_8\Big(L^2+4\Big)+2c_6-c_7\Big)\frac{A_0'A_0''}{r^3} \\
& -\Big(c_8\Big(2L^2+5\Big)+8c_6-2c_7\Big)\frac{A_0'A_0^{(3)}}{r^2}-2\Big(c_8\Big(L^2+4\Big)+4c_6\Big)\frac{(A_0'')^2}{r^2}+(-4c_6+2c_7+c_8)\frac{\omega^2(A_0')^2}{r^2} \\
& -\frac{A_0'}{r}\Big((4c_6+2c_7+c_8)\omega^2A_0''+(-4c_6+4c_7+3c_8)A_0^{(4)}\Big)+\frac{3(4c_6-3c_8)A_0^{(3)}A_0''}{r} \\
& +2\Big((c_6+c_8)A_0'A_0^{(5)}+(4c_6-c_8)A_0''A_0^{(4)}+(3c_6-2c_8)(A_0^{(3)})^2\Big) \\
& +\omega^2\Big((2c_7+3c_8)A_0'A_0^{(3)}+c_8(A_0'')^2\Big),
\end{aligned}
\tag{A.5}
$$

$$
\begin{aligned}
d_2 = {} & \Big((2c_6+c_8)L^2-6c_7+6c_8\Big)\frac{(A_0')^2}{r^3}-\Big(c_8\Big(L^2+2\Big)+16c_6-8c_7\Big)\frac{A_0'A_0''}{r^2} \\
& -\frac{2}{r}\Big((2c_6+c_8)\omega^2(A_0')^2+(c_6+3c_7-2c_8)A_0'A_0^{(3)}+(c_7-2c_8)(A_0'')^2\Big) \\
& +A_0'\Big(2c_8\omega^2A_0''+(2c_6+4c_7+7c_8)A_0^{(4)}\Big)+2(3c_6+2c_7+3c_8)A_0''A_0^{(3)},
\end{aligned}
\tag{A.6}
$$

$$
d_3 = (-4c_6+2c_7+c_8)\frac{(A_0')^2}{r^2}-(4c_6+2c_7+c_8)\frac{A_0'A_0''}{r}+2(2c_7+3c_8)A_0'A_0^{(3)}+2c_8(A_0'')^2, \tag{A.7}
$$

$$
d_4 = c_8A_0'A_0''-(2c_6+c_8)\frac{(A_0')^2}{r}. \tag{A.8}
$$

Note that we only need to go up to order $1/\Lambda^8$ for the terms c_1^2, c_1c_2 and c_2^2 in order to get the ϵ_1^4 contributions at leading order. In terms of this new variable we find that the constraint is given by

$$
v_1^\ell = 0\,. \tag{A.9}
$$

JHEP06(2024)146

B Explicit expressions for propagation around spherically symmetric backgrounds

The equations of motion for the propagating modes are given by eq. (4.13) with $W_{I,\ell}$ given by

$$\begin{aligned}
W_{2,\ell} &= 1-\frac{B^2}{R^2}+16\epsilon_1^2\frac{B^2}{R^2}(2c_1+c_2)f'(R)^2 \\
&\quad+2\epsilon_1^2\epsilon_2^2\Bigg\{(-5c_3+c_4+2c_5)\frac{B^2}{R^2}\frac{f'(R)^2}{R^2}+\left(\frac{B^2}{R^2}(7c_3+c_4+2c_5)-4c_3\right)f''(R)^2 \\
&\qquad-2\left(\left(\frac{B^2}{R^2}(c_3+c_4+2c_5)+3c_3\right)f''(R)+2c_3\left(1-2\frac{B^2}{R^2}\right)Rf^{(3)}(R)\right)\frac{f'(R)}{R}\Bigg\} \\
&\quad+2\epsilon_1^2\epsilon_2^2\Omega^2(2c_6-c_8)\frac{B^2}{R^2}\Bigg\{\left(2\frac{B^2}{R^2}-1\right)\frac{f'(R)^2}{R^2}+\left(1-\frac{B^2}{R^2}\right)f''(R)^2 \\
&\qquad-\left(\frac{B^2}{R^2}f''(R)+\left(1-\frac{B^2}{R^2}\right)Rf^{(3)}\right)\frac{f'(R)}{R}\Bigg\},
\end{aligned} \tag{B.1}$$

and

$$\begin{aligned}
W_{4,\ell} &= 1-\frac{B^2}{R^2}+8\epsilon_1^2\frac{B^2}{R^2}c_2f'(R)^2 \\
&\quad+2\epsilon_1^2\epsilon_2^2\Bigg\{(-3c_3+c_4)\frac{B^2}{R^2}\frac{f'(R)^2}{R^2}+\left(\frac{B^2}{R^2}(c_3-c_4)-4c_3\right)f''(R)^2 \\
&\qquad+\left(2c_3\left(\frac{B^2}{R^2}-3\right)f''(R)+\left(\frac{B^2}{R^2}(c_3-c_4)-4c_3\right)Rf^{(3)}(R)\right)\frac{f'(R)}{R}\Bigg\} \\
&\quad-2\epsilon_1^2\epsilon_2^2\Omega^2c_8\frac{B^2}{R^2}\Bigg\{\left(2\frac{B^2}{R^2}-1\right)\frac{f'(R)^2}{R^2}+\left(1-\frac{B^2}{R^2}\right)f''(R)^2 \\
&\qquad-\left(\frac{B^2}{R^2}f''(R)+\left(1-\frac{B^2}{R^2}\right)Rf^{(3)}\right)\frac{f'(R)}{R}\Bigg\}.
\end{aligned} \tag{B.2}$$

Let us now write down the turning point for both physical modes

$$R^t_{I,\ell}=B\left[1-\epsilon_1^2\Psi^{(1)}_{I,\ell}(B)-\epsilon_1^2\epsilon_2^2\Psi^{(2)}_{I,\ell}(B)-\epsilon_1^2\epsilon_2^2\Omega^2\Psi^{(3)}_{I,\ell}(B)\right], \tag{B.3}$$

where

$$\begin{aligned}
\Psi^{(1)}_{2,\ell}(B)&=8(2c_1+c_2)f'(B)^2=(f_2+g_2)f'(B)^2, \\
\Psi^{(2)}_{2,\ell}(B)&=-(5c_3-c_4-2c_5)\frac{f'(B)^2}{B^2}-2(4c_3+c_4+2c_5)\frac{f'(B)f''(B)}{B}+(3c_3+c_4+2c_5)f''(B)^2 \\
&\quad+4c_3f'(B)f^{(3)}(B) \\
&=-\frac{1}{3}\Bigg\{(f_3+3(g_3-4h_3))\frac{f'(B)^2}{B^2}-2(f_3+3(g_3+2h_3))\frac{f'(B)f''(B)}{B} \\
&\quad+(f_3+3g_3+4h_3)f''(B)^2+8h_3f'(B)f^{(3)}(B)\Bigg\}, \\
\Psi^{(3)}_{2,\ell}(B)&=(2c_6-c_8)\left(\frac{f'(B)^2}{B^2}-\frac{f'(B)f''(B)}{B}\right)=2(2f_4+g_4)\left(\frac{f'(B)^2}{B^2}-\frac{f'(B)f''(B)}{B}\right),
\end{aligned}$$

JHEP06(2024)146

and

$$\begin{aligned}
\Psi^{(1)}_{4,\ell}(B) &= 4c_2 f'(B)^2 = -(f_2 - g_2) f'(B)^2\,, \\
\Psi^{(2)}_{4,\ell}(B) &= -(3c_3 - c_4)\frac{f'(B)^2}{B^2} - 4c_3\frac{f'(B)f''(B)}{B} - (3c_3 + c_4)\Big(f''(B)^2 + f'(B)f^{(3)}(B)\Big) \\
&= \frac{1}{3}\Bigg\{-(f_3 - 3g_3 - 8h_3)\frac{f'(B)^2}{B^2} + 8h_3\frac{f'(B)f''(B)}{B} \\
&\qquad + (f_3 - 3g_3 + 4h_3)\Big(f''(B)^2 + f'(B)f^{(3)}(B)\Big)\Bigg\}\,, \\
\Psi^{(3)}_{4,\ell}(B) &= -c_8\left(\frac{f'(B)^2}{B^2} - \frac{f'(B)f''(B)}{B}\right) = -2(2f_4 - g_4)\left(\frac{f'(B)^2}{B^2} - \frac{f'(B)f''(B)}{B}\right),
\end{aligned} \tag{B.4}$$

where, in the last equalities, we have converted the Wilson coefficients from the Lagrangian to the scattering amplitude parameters by using eq. (2.5). The functions $U_{I,\ell}$ appearing in the phase shift and time delay expressions are given by

$$\begin{aligned}
U_{I,\ell} = \frac{B^2}{R^2}\Big[\epsilon_1^2\Big(\Psi^{(1)}_{I,\ell}(R) - \Psi^{(1)}_{I,\ell}(B)\Big) + \epsilon_1^2\epsilon_2^2\Big(\Psi^{(2)}_{I,\ell}(R) - \Psi^{(2)}_{I,\ell}(B)\Big) + \epsilon_1^2\epsilon_2^2\Omega^2\Big(\Psi^{(3)}_{I,\ell}(R) - \Psi^{(3)}_{I,\ell}(B)\Big)\Big] \\
+ \left(1 - \frac{B^2}{R^2}\right)\Big(\epsilon_1^2\epsilon_2^2\Upsilon^{(1)}_{I,\ell}(R) + \epsilon_1^2\epsilon_2^2\Omega^2\Upsilon^{(2)}_{I,\ell}(R)\Big)\,,
\end{aligned} \tag{B.5}$$

where it is clear that the first term in square bracket vanishes when $R \to B$ which ensures the convergence of the time delay. The analytical expressions for the functions entering eq. (B.5) above are given by

$$\begin{aligned}
\Upsilon^{(1)}_{2,\ell}(R) &= -2c_3\left(3\frac{f'(R)f''(R)}{R} + 2\Big(f''(R)^2 + f'(R)f^{(3)}(R)\Big)\right) \\
&= \frac{4}{3}h_3\left(3\frac{f'(R)f''(R)}{R} + 2\Big(f''(R)^2 + f'(R)f^{(3)}(R)\Big)\right), \\
\Upsilon^{(2)}_{2,\ell}(R) &= -(2c_6 - c_8)\left\{2\frac{f'(R)^2}{R^2} - \frac{f'(R)f''(R)}{R} - f''(R)^2 + f'(R)f^{(3)}(R)\right\} \\
&= -2(2f_4 + g_4)\left\{2\frac{f'(R)^2}{R^2} - \frac{f'(R)f''(R)}{R} - f''(R)^2 + f'(R)f^{(3)}(R)\right\},
\end{aligned} \tag{B.6}$$

and

$$\begin{aligned}
\Upsilon^{(1)}_{4,\ell}(R) &= \Upsilon^{(1)}_{2,\ell}(R)\,, \\
\Upsilon^{(2)}_{4,\ell}(R) &= c_8\left\{2\frac{f'(R)^2}{R^2} - \frac{f'(R)f''(R)}{R} - f''(R)^2 + f'(R)f^{(3)}(R)\right\} \\
&= 2(2f_4 - g_4))\left\{2\frac{f'(R)^2}{R^2} - \frac{f'(R)f''(R)}{R} - f''(R)^2 + f'(R)f^{(3)}(R)\right\}.
\end{aligned} \tag{B.7}$$

JHEP06(2024)146

Finally, the expression for the time delay is

$$
\begin{aligned}
&(\omega\Delta T_{b,I,\ell}(\omega))\\
&= 2(\omega r_0)\left[\int_B^\infty \frac{\partial_\omega(\omega U_{I,\ell}(R))}{\sqrt{1-\frac{B^2}{R^2}}}\mathrm{d}R + \frac{\pi}{2}\Big(B - \partial_\omega\Big(\omega R^t_{I,\ell}\Big)\Big)\right]\\
&= 2(\omega r_0)\left[\int_B^\infty \frac{B^2}{R^2}\frac{\Big[\epsilon_1^2\Psi^{(1)}_{I,\ell}(R) + \epsilon_1^2\epsilon_2^2\Psi^{(2)}_{I,\ell}(R) + 3\epsilon_1^2\epsilon_2^2\Omega^2\Psi^{(3)}_{I,\ell}(R)\Big] - \Big[R\leftrightarrow B\Big]}{\sqrt{1-\frac{B^2}{R^2}}}\mathrm{d}R\right.\\
&\qquad + \int_B^\infty \sqrt{1-\frac{B^2}{R^2}}\left(\epsilon_1^2\epsilon_2^2\Upsilon^{(1)}_{I,\ell}(R) + 3\epsilon_1^2\epsilon_2^2\Omega^2\frac{B^2}{R^2}\Upsilon^{(2)}_{I,\ell}(R)\right)\mathrm{d}R\\
&\qquad \left. + \frac{\pi}{2}B\Big(\epsilon_1^2\Psi^{(1)}_{I,\ell} + \epsilon_1^2\epsilon_2^2\Psi^{(2)}_{I,\ell} + 3\epsilon_1^2\epsilon_2^2\Omega^2\Psi^{(3)}_{I,\ell}\Big)\right]\\
&= 2(\omega r_0)\left[\int_B^\infty \frac{B^2}{R^2}\frac{\Big[\epsilon_1^2\Psi^{(1)}_{I,\ell}(R) + \epsilon_1^2\epsilon_2^2\Psi^{(2)}_{I,\ell}(R) + 3\epsilon_1^2\epsilon_2^2\Omega^2\Psi^{(3)}_{I,\ell}(R)\Big]}{\sqrt{1-\frac{B^2}{R^2}}}\mathrm{d}R\right.\\
&\qquad \left. + \int_B^\infty \sqrt{1-\frac{B^2}{R^2}}\left(\epsilon_1^2\epsilon_2^2\Upsilon^{(1)}_{I,\ell}(R) + 3\epsilon_1^2\epsilon_2^2\Omega^2\frac{B^2}{R^2}\Upsilon^{(2)}_{I,\ell}(R)\right)\mathrm{d}R\right].
\end{aligned}
\tag{B.8}
$$

Note that the integral over the constant $\Psi^{(j)}_{I,\ell}(B)$ can be performed and exactly cancels out the extra term that is free of any integration.

C Optimization method

We describe here the algorithm used to optimize the causality bounds. For any two-dimensional plot in the $(\mathcal{W}_J, \mathcal{W}_K)$-plane, we start by fixing all the remaining coefficients collectively denoted by $\{\mathcal{W}_L\}$ to constants corresponding to a particular UV completion or another interesting case. This is necessary in order to reduce the complexity of the optimization by only allowing 2 of the 8 coefficients to vary.[10]

The vector causality constraints reduce to 2 constraints in the even and odd sector and the extremization procedure can be done in each independently. When presenting the results, we can choose to show the causality bounds of each sector individually or to show the final result which is achieved by taking their union. In the following, we forget about the two sectors and assume we are specialising to a given one, only to take the union of both at the end.

The boundary of the causality constraint reads $(\omega\Delta T) = -1$ and can be solved for $\mathcal{W}_J$ as a function of $\mathcal{W}_K$ and all the other parameters of the problem (other Wilson coefficients, background parameters, and parameters defining the validity of the EFT and WKB expansions). Next, we discretise the direction $\mathcal{W}_K$ by letting this coefficient take values in the interval $\left[\mathcal{W}_K^{(\min)}, \mathcal{W}_K^{(\max)}\right]$ divided in n_K equal steps of length $\Delta\mathcal{W}_K = (\mathcal{W}_K^{(\max)} - \mathcal{W}_K^{(\min)})/n_K$,

$$
\mathcal{W}_K = \left\{\mathcal{W}_K^{(\min)}, \mathcal{W}_K^{(\min)} + \Delta\mathcal{W}_K, \cdots, \mathcal{W}_K^{(\max)}\right\}. \tag{C.1}
$$

[10] Note however that the causality bounds derived in this paper are insensitive to g_4' and that g_2 is set to either 1 or 0 without loss of generality.

JHEP06(2024)146

For each such value of $\mathcal{W}_K$, we find the maximal (if it exists) value that $\mathcal{W}_J$ can take by extremizing over the parameters of the background profile and the ones controlling the EFT expansion, under the constraint that one remains in the regime of validity of the EFT and the WKB approximations simultaneously. This way, we get a set of extremal parameters per discretised value of $\mathcal{W}_K$ that we plug back into the equation $(\omega\Delta T) = -1$, which in turn gives an optimised straight line in the $(\mathcal{W}_J, \mathcal{W}_K)$-plane separating the causality-violating region from the allowed one. One gets such a line for each discretised value of $\mathcal{W}_K$ and hence can form an envelope by imposing all the constraints derived in this way. This procedure gives an upper (lower) bound on $\mathcal{W}_J$ when the coefficient in front of $\mathcal{W}_J$ is negative (positive). Since in some cases, the coefficient is not sign-definite (as seen in table 2), we obtain but upper and lower bounds. Finally, we refine our bounds by performing the same procedure once again after swapping the role of $\mathcal{W}_J$ and $\mathcal{W}_K$, i.e. discretising the other axis and getting left/right bounds rather than upper/lower.

As mentioned earlier, this is done independently in the even and odd sectors of the vector. The theory is only causal if neither mode propagate in a causality-violating way, hence the final causality bounds are obtained by imposing causality on both sectors simultaneously.

D Spin-2 partial UV (in)completions

Here, we focus on the partial UV (in)completions suggested in [77]. These are constructed by on-shell amplitude methods and requirements on the Regge behaviour. First, they construct the residue at the spin-2 pole and split this in two cases: parity even and odd. They allow for the freedom of adding arbitrary contact terms which are then fixed so that the amplitude has the desired Regge limit (growing as $\mathcal{O}(s^2, u^2, t^2)$). Without taking into account these additional contributions from contact terms, the even and odd partial UV completions only propagate even or odd modes, but these additional contact terms do not respect the parity and the partial UV completions in [77] propagate both even and odd modes. From a Lagrangian perspective, the construction of [77] includes higher derivative couplings between the photon and the massive spin-2 field.

The causality and positivity bounds for four different spin-2 partial UV (in)completions are presented in figure 23. According to table 1, all dimension-8 and 10 free coefficients (i.e. with the exception of f_2 and g_3 in this specific case) are identical in each of the four proposed partial UV completions. For the two UV completions that are causal, they also lie within the positivity bounds and so are consistent UV completions. The remaining two possible 'UV completions' (on the right side) which do not satisfy causality, also do not satisfy positivity as there is in fact no region allowed by positivity in the slice in which they live. We highlight again that the causality bounds do not require any UV assumptions. In other words, the implications of our result are that the non-minimal coupling between the photon and the spin-2 in these partial UV completions leads to acausal propagation.

The fact that these spin-2 partial UV (in)completions lie outside positivity bounds was already observed in [77]. Note that the fact that spin-2 fields lead to an s^2 growth of the amplitude is not the reason why positivity bounds fail. The Froissart-like bound requirement that the amplitude should grow strictly softer than s^2 is a requirement in the $|s| \to \infty$ limit, that is, in the full UV theory not on the EFT nor the partial UV completion. Just as is

JHEP06(2024)146

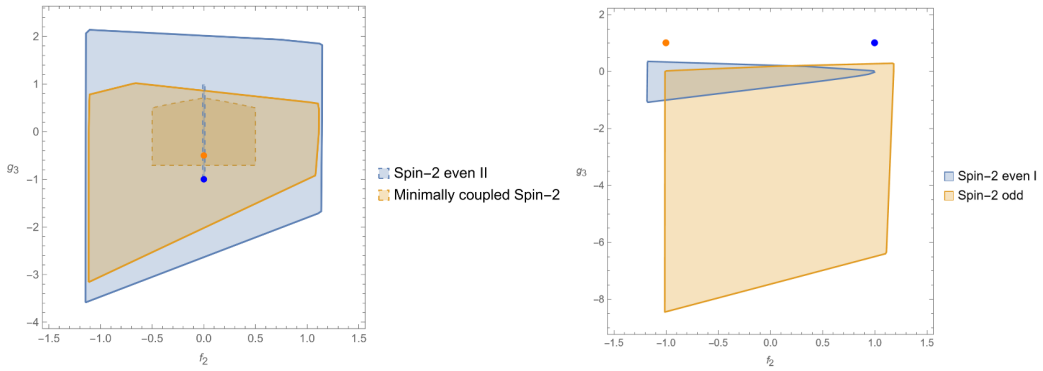

Figure 23. Causality (thick line) and positivity (dashed line) bounds in the (f_2, g_3) plane with all other coefficients set to the values of the corresponding partial UV completions as in table 1. On the left side, we have $f_3 = h_3 = f_4 = 0$ for both regions and $g_4 = 1$ and $1/2$ for the blue and orange regions respectively. Meanwhile, the right panel has $f_3 = h_3 = 0$, $g_4 = 1$ for both regions and $f_4 = 1/2$ and $-1/2$ for the blue and orange regions respectively. The partial UV completions with causal propagation appear on the left whereas the ones on the right do not agree with either of the causality or positivity bounds. In the left-hand plot the parameter values for the spin-2 even UV completion give an allowed region that is described by $f_2 = 0 \cup |g_3| < 1$ giving a one-dimensional region, depicted as a slim two-dimensional region for visibility. On the right-hand plot, there is no region allowed by positivity bounds.

the case of gravity, when considering massive spin-2 fields coupled to photons, we can also assume that at very high energies there is a UV completion with the desired behavior.

E Reducing the angle dependence for the positivity bounds

Linear positivity bounds for indefinite helicity amplitudes typically have the form

$$\begin{aligned} &A_1 + A_2 \cos(2\theta)\cos(2\chi) + A_3(\cos\phi \sin(2\theta) + \cos\phi \sin(2\chi)) + \\ &+ A_4 \cos(\phi - \psi)\sin(2\theta)\sin(2\chi) + A_5 \cos(\phi + \psi)\sin(2\theta)\sin(2\chi) > 0, \end{aligned} \tag{E.1}$$

which must be valid for all values of angles ϕ, ψ, χ, θ. This requirement implies several non-linear bounds on the coefficients A_1, A_2, A_3, A_4, A_4 depending on the coupling constants.

Taking the particular case $\theta = 0$ one obtains

$$A_1 + A_2 \cos(2\chi) + A_3 \cos\psi \sin(2\chi) > 0. \tag{E.2}$$

This can be transformed to

$$A_1 + \sqrt{A_2^2 + A_3^2 \cos^2\psi}\cos(2\chi + \chi_0) > 0. \tag{E.3}$$

Here χ_0 depends on A_2, A_3 but the concrete expression is irrelevant for the derivation. The strongest bound corresponds to $\cos(2\chi + \chi_0) = -1$. Thus,

$$A_1 - \sqrt{A_2^2 + A_3^2 \cos^2\psi} > 0, \tag{E.4}$$

or

$$A_1^2 > A_2^2 + A_3^2 \cos^2\psi. \tag{E.5}$$

JHEP06(2024)146

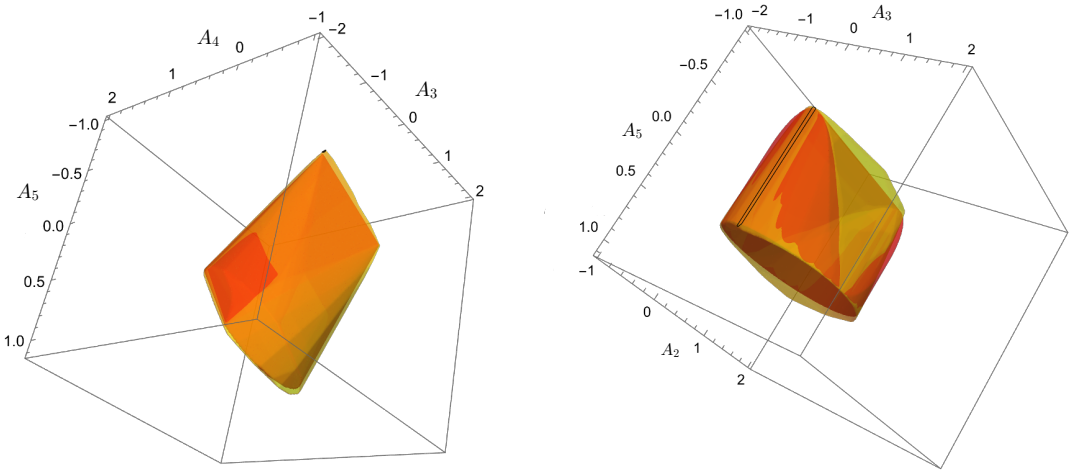

(a) (b)

Figure 24. (a) Allowed region for $A_3,\ A_4,\ A_5$ when $A_1 = 1$ and $A_2 = 1/2$ are taken. The red volume presents the analytic bound while the yellow area corresponds to the result of numerical optimization of angles. (b) Allowed region for $A_2,\ A_3,\ A_5$ for $A_1 = 1,\ A_4 = 1/2$. The meaning of the colours is the same as in the plot (a).

This condition is satisfied for any ψ if

$$A_1^2 > A_2^2 + A_3^2. \tag{E.6}$$

Thus, the angle dependence is completely reduced and the obtained condition is a non-linear bound on the couplings. However, numerical analysis shows that eq. (E.1) in fact leads to stronger constraints than eq. (E.6). To derive them, it seems to be enough to take $\theta = \chi = \pi/4$,

$$A_1 + A_3(\cos\phi + \cos\psi) + A_4\cos(\phi - \psi) + A_5\cos(\phi + \psi) > 0, \tag{E.7}$$

or

$$A_1 + A_3\cos\psi + \cos\phi(A_3 + (A4 + A5)\cos\psi) + \sin\phi\sin\psi(A_4 - A_5) > 0. \tag{E.8}$$

Repeating the previous procedure we obtain

$$(A_1 + A_3\cos\psi)^2 - (A_3 + (A4 + A5)\cos\psi)^2 - \sin^2\psi(A_4 - A_5)^2 > 0. \tag{E.9}$$

After some simplifications, one can get

$$(A_3^2 - A_4A_5)y^2 + 2(A_1A_2 - 2A_3(A_4 + A_5))y + A_1^2 - A_3^2 - A_4^2 + 2A_4A_5 - A_5^2 > 0. \tag{E.10}$$

Here $y = \cos\psi$ is between -1 and 1. This bound can be brought to the form

$$Ay^2 + By + C > 0\,. \tag{E.11}$$

This is satisfied for all angles if one of the following four conditions is satisfied,

- $A > 0,\ D = B^2 - 4AC < 0,$

JHEP06(2024)146

- $A < 0$, $D > 0$ and $x_1 < -1$ and $x_2 > 1$ where $x_1 < x_2$ are two real roots of the quadratic polynomial,
- $D > 0$, $A > 0$, $x_1 < -1$ or $x_2 > 1$,
- $A = 0$, $\mid B \mid < C$.

In figure 24 we show the coincidence of the allowed ranges obtained by numerical scanning over angles and analytic result described here. The numerical region (yellow-shaded) is a bit wider reflecting the fact that scanning does not always provide the optimal angles for the strongest bound.

F Comparison of conventions with other works

In this appendix, we provide a conversion chart that enables the reader to go from our conventions to the ones of [75, 76] and [77].

EFT dim	This Paper	[75, 76]	[77]
8	c_1	$f_2 = 8c_1 + 2c_2$	$f_2 = 8c_1 + 2c_2$
	c_2	$g_2 = 8c_1 + 6c_2$	$g_2 = 8c_1 + 6c_2$
10	c_3	$f_3 = -3(c_3 + c_4 + c_5)$	$f_3 = -3(c_3 + c_4 + c_5)$
	c_4	$g_3 = -c_5$	$g_3 = -c_5$
	c_5	$h_3 = -\frac{3}{2}c_3$	$h_3 = -\frac{3}{2}c_3$
12	c_6	$f_4 = \frac{1}{4}c_6$	$f_4 = \frac{1}{4}c_6$
	c_7	$g_{4,1} = \frac{1}{2}(c_6 + c_8) + c_7$	$g_4 = \frac{1}{2}(c_6 - c_8)$
	c_8	$g_{4,2} = -\frac{1}{2}(c_7 + c_8)$	$g_4' = c_7 + c_8$

Table 4. Conversion table for the EFT coefficients.

References

[1] A. Adams et al., *Causality, analyticity and an IR obstruction to UV completion*, *JHEP* **10** (2006) 014 [hep-th/0602178] [INSPIRE].

[2] M.R. Pennington and J. Portoles, *The Chiral Lagrangian parameters, l1, l2, are determined by the rho resonance*, *Phys. Lett. B* **344** (1995) 399 [hep-ph/9409426] [INSPIRE].

[3] T.N. Pham and T.N. Truong, *Evaluation of the Derivative Quartic Terms of the Meson Chiral Lagrangian From Forward Dispersion Relation*, *Phys. Rev. D* **31** (1985) 3027 [INSPIRE].

[4] R.J. Eden, P.V. Landshoff, D.I. Olive and J.C. Polkinghorne, *The analytic S-matrix*, Cambridge University Press (1966).

JHEP06(2024)146

[5] A. Martin, *Scattering Theory: Unitarity, Analyticity and Crossing*, vol. 3, Springer (1969) [DOI:10.1007/BFb0101043] [INSPIRE].

[6] M.F. Paulos et al., *The S-matrix bootstrap. Part I: QFT in AdS*, *JHEP* **11** (2017) 133 [arXiv:1607.06109] [INSPIRE].

[7] M. Kruczenski, J. Penedones and B.C. van Rees, *Snowmass White Paper: S-matrix Bootstrap*, arXiv:2203.02421 [INSPIRE].

[8] L. Vecchi, *Causal versus analytic constraints on anomalous quartic gauge couplings*, *JHEP* **11** (2007) 054 [arXiv:0704.1900] [INSPIRE].

[9] C. de Rham, S. Melville, A.J. Tolley and S.-Y. Zhou, *Positivity bounds for scalar field theories*, *Phys. Rev. D* **96** (2017) 081702 [arXiv:1702.06134] [INSPIRE].

[10] A.V. Manohar and V. Mateu, *Dispersion Relation Bounds for $\pi\pi$ Scattering*, *Phys. Rev. D* **77** (2008) 094019 [arXiv:0801.3222] [INSPIRE].

[11] A. Nicolis, R. Rattazzi and E. Trincherini, *Energy's and amplitudes' positivity*, *JHEP* **05** (2010) 095 [*Erratum ibid.* **11** (2011) 128] [arXiv:0912.4258] [INSPIRE].

[12] B. Bellazzini, *Softness and amplitudes' positivity for spinning particles*, *JHEP* **02** (2017) 034 [arXiv:1605.06111] [INSPIRE].

[13] C. de Rham, S. Melville, A.J. Tolley and S.-Y. Zhou, *UV complete me: Positivity Bounds for Particles with Spin*, *JHEP* **03** (2018) 011 [arXiv:1706.02712] [INSPIRE].

[14] J. Bonifacio, K. Hinterbichler and R.A. Rosen, *Positivity constraints for pseudolinear massive spin-2 and vector Galileons*, *Phys. Rev. D* **94** (2016) 104001 [arXiv:1607.06084] [INSPIRE].

[15] L. Alberte et al., *Positivity Constraints on Interacting Pseudo-Linear Spin-2 Fields*, *JHEP* **07** (2020) 121 [arXiv:1912.10018] [INSPIRE].

[16] L. Alberte et al., *Positivity Constraints on Interacting Spin-2 Fields*, *JHEP* **03** (2020) 097 [arXiv:1910.11799] [INSPIRE].

[17] Z.-Y. Wang, C. Zhang and S.-Y. Zhou, *Generalized elastic positivity bounds on interacting massive spin-2 theories*, *JHEP* **04** (2021) 217 [arXiv:2011.05190] [INSPIRE].

[18] J. Davighi, S. Melville and T. You, *Natural selection rules: new positivity bounds for massive spinning particles*, *JHEP* **02** (2022) 167 [arXiv:2108.06334] [INSPIRE].

[19] B. Bellazzini, F. Riva, J. Serra and F. Sgarlata, *Massive Higher Spins: Effective Theory and Consistency*, *JHEP* **10** (2019) 189 [arXiv:1903.08664] [INSPIRE].

[20] K. Häring and A. Zhiboedov, *Gravitational Regge bounds*, *SciPost Phys.* **16** (2024) 034 [arXiv:2202.08280] [INSPIRE].

[21] Z. Bern, D. Kosmopoulos and A. Zhiboedov, *Gravitational effective field theory islands, low-spin dominance, and the four-graviton amplitude*, *J. Phys. A* **54** (2021) 344002 [arXiv:2103.12728] [INSPIRE].

[22] S.D. Chowdhury et al., *Crossing Symmetric Spinning S-matrix Bootstrap: EFT bounds*, *SciPost Phys.* **13** (2022) 051 [arXiv:2112.11755] [INSPIRE].

[23] L.-Y. Chiang et al., *(Non)-projective bounds on gravitational EFT*, arXiv:2201.07177 [INSPIRE].

[24] L. Alberte, C. de Rham, S. Jaitly and A.J. Tolley, *Positivity Bounds and the Massless Spin-2 Pole*, *Phys. Rev. D* **102** (2020) 125023 [arXiv:2007.12667] [INSPIRE].

[25] L. Alberte, C. de Rham, S. Jaitly and A.J. Tolley, *QED positivity bounds*, *Phys. Rev. D* **103** (2021) 125020 [arXiv:2012.05798] [INSPIRE].

JHEP06(2024)146

[26] L. Alberte, C. de Rham, S. Jaitly and A.J. Tolley, *Reverse Bootstrapping: IR Lessons for UV Physics*, *Phys. Rev. Lett.* **128** (2022) 051602 [arXiv:2111.09226] [INSPIRE].

[27] C. de Rham, S. Jaitly and A.J. Tolley, *Constraints on Regge behavior from IR physics*, *Phys. Rev. D* **108** (2023) 046011 [arXiv:2212.04975] [INSPIRE].

[28] Y. Hamada, T. Noumi and G. Shiu, *Weak Gravity Conjecture from Unitarity and Causality*, *Phys. Rev. Lett.* **123** (2019) 051601 [arXiv:1810.03637] [INSPIRE].

[29] T. Noumi and J. Tokuda, *Finite energy sum rules for gravitational Regge amplitudes*, *JHEP* **06** (2023) 032 [arXiv:2212.08001] [INSPIRE].

[30] J. Tokuda, K. Aoki and S. Hirano, *Gravitational positivity bounds*, *JHEP* **11** (2020) 054 [arXiv:2007.15009] [INSPIRE].

[31] M. Herrero-Valea, R. Santos-Garcia and A. Tokareva, *Massless positivity in graviton exchange*, *Phys. Rev. D* **104** (2021) 085022 [arXiv:2011.11652] [INSPIRE].

[32] M. Herrero-Valea, A.S. Koshelev and A. Tokareva, *UV graviton scattering and positivity bounds from IR dispersion relations*, *Phys. Rev. D* **106** (2022) 105002 [arXiv:2205.13332] [INSPIRE].

[33] C. Cheung and G.N. Remmen, *Positive Signs in Massive Gravity*, *JHEP* **04** (2016) 002 [arXiv:1601.04068] [INSPIRE].

[34] B. Bellazzini, F. Riva, J. Serra and F. Sgarlata, *Beyond Positivity Bounds and the Fate of Massive Gravity*, *Phys. Rev. Lett.* **120** (2018) 161101 [arXiv:1710.02539] [INSPIRE].

[35] C. de Rham, S. Melville and A.J. Tolley, *Improved Positivity Bounds and Massive Gravity*, *JHEP* **04** (2018) 083 [arXiv:1710.09611] [INSPIRE].

[36] B. Bellazzini, G. Isabella, S. Ricossa and F. Riva, *Massive gravity is not positive*, *Phys. Rev. D* **109** (2024) 024051 [arXiv:2304.02550] [INSPIRE].

[37] L.-Y. Chiang et al., *Into the EFThedron and UV constraints from IR consistency*, *JHEP* **03** (2022) 063 [arXiv:2105.02862] [INSPIRE].

[38] N. Arkani-Hamed, T.-C. Huang and Y.-T. Huang, *The EFT-Hedron*, *JHEP* **05** (2021) 259 [arXiv:2012.15849] [INSPIRE].

[39] B. Bellazzini et al., *Positive moments for scattering amplitudes*, *Phys. Rev. D* **104** (2021) 036006 [arXiv:2011.00037] [INSPIRE].

[40] A.J. Tolley, Z.-Y. Wang and S.-Y. Zhou, *New positivity bounds from full crossing symmetry*, *JHEP* **05** (2021) 255 [arXiv:2011.02400] [INSPIRE].

[41] S. Caron-Huot and V. Van Duong, *Extremal Effective Field Theories*, *JHEP* **05** (2021) 280 [arXiv:2011.02957] [INSPIRE].

[42] C. Zhang and S.-Y. Zhou, *Positivity bounds on vector boson scattering at the LHC*, *Phys. Rev. D* **100** (2019) 095003 [arXiv:1808.00010] [INSPIRE].

[43] Q. Bi, C. Zhang and S.-Y. Zhou, *Positivity constraints on aQGC: carving out the physical parameter space*, *JHEP* **06** (2019) 137 [arXiv:1902.08977] [INSPIRE].

[44] G.N. Remmen and N.L. Rodd, *Consistency of the Standard Model Effective Field Theory*, *JHEP* **12** (2019) 032 [arXiv:1908.09845] [INSPIRE].

[45] C. Zhang and S.-Y. Zhou, *Convex Geometry Perspective on the (Standard Model) Effective Field Theory Space*, *Phys. Rev. Lett.* **125** (2020) 201601 [arXiv:2005.03047] [INSPIRE].

JHEP06(2024)146

[46] B. Fuks, Y. Liu, C. Zhang and S.-Y. Zhou, *Positivity in electron-positron scattering: testing the axiomatic quantum field theory principles and probing the existence of UV states*, *Chin. Phys. C* **45** (2021) 023108 [arXiv:2009.02212] [INSPIRE].

[47] G.N. Remmen and N.L. Rodd, *Flavor Constraints from Unitarity and Analyticity*, *Phys. Rev. Lett.* **125** (2020) 081601 [*Erratum ibid.* **127** (2021) 149901] [arXiv:2004.02885] [INSPIRE].

[48] K. Yamashita, C. Zhang and S.-Y. Zhou, *Elastic positivity vs extremal positivity bounds in SMEFT: a case study in transversal electroweak gauge-boson scatterings*, *JHEP* **01** (2021) 095 [arXiv:2009.04490] [INSPIRE].

[49] D. Ghosh, R. Sharma and F. Ullah, *Amplitude's positivity vs. subluminality: causality and unitarity constraints on dimension 6 & 8 gluonic operators in the SMEFT*, *JHEP* **02** (2023) 199 [arXiv:2211.01322] [INSPIRE].

[50] N.N. Bogolyubov and D.V. Shirkov, *Introduction to the theory of quantized fields*, *Intersci. Monogr. Phys. Astron.* **3** (1959) 1 [INSPIRE].

[51] J.S. Toll, *Causality and the Dispersion Relation: Logical Foundations*, *Phys. Rev.* **104** (1956) 1760 [INSPIRE].

[52] H.J. Bremermann, R. Oehme and J.G. Taylor, *Proof of Dispersion Relations in Quantized Field Theories*, *Phys. Rev.* **109** (1958) 2178 [INSPIRE].

[53] N.N. Bogoliubov, D.V. Shirkov and E.M. Henley, *Introduction to the Theory of Quantized Fields*, *Phys. Today* **13** (1960) 40.

[54] K. Hepp, *On the analyticity properties of the scattering amplitude in relativistic quantum field theory*, *Helv. Phys. Acta* **37** (1964) 639.

[55] J.-P. Bruneton, *On causality and superluminal behavior in classical field theories: Applications to k-essence theories and MOND-like theories of gravity*, *Phys. Rev. D* **75** (2007) 085013 [gr-qc/0607055] [INSPIRE].

[56] J.-P. Bruneton and G. Esposito-Farese, *Field-theoretical formulations of MOND-like gravity*, *Phys. Rev. D* **76** (2007) 124012 [*Erratum ibid.* **76** (2007) 129902] [arXiv:0705.4043] [INSPIRE].

[57] E. Babichev, V. Mukhanov and A. Vikman, *k-Essence, superluminal propagation, causality and emergent geometry*, *JHEP* **02** (2008) 101 [arXiv:0708.0561] [INSPIRE].

[58] X.O. Camanho, J.D. Edelstein, J. Maldacena and A. Zhiboedov, *Causality Constraints on Corrections to the Graviton Three-Point Coupling*, *JHEP* **02** (2016) 020 [arXiv:1407.5597] [INSPIRE].

[59] X.O. Camanho, G. Lucena Gómez and R. Rahman, *Causality Constraints on Massive Gravity*, *Phys. Rev. D* **96** (2017) 084007 [arXiv:1610.02033] [INSPIRE].

[60] D. Bai and Y.-H. Xing, *Higher Derivative Theories for Interacting Massless Gravitons in Minkowski Spacetime*, *Nucl. Phys. B* **932** (2018) 15 [arXiv:1610.00241] [INSPIRE].

[61] G. Goon and K. Hinterbichler, *Superluminality, black holes and EFT*, *JHEP* **02** (2017) 134 [arXiv:1609.00723] [INSPIRE].

[62] K. Hinterbichler, A. Joyce and R.A. Rosen, *Eikonal scattering and asymptotic superluminality of massless higher spin fields*, *Phys. Rev. D* **97** (2018) 125019 [arXiv:1712.10021] [INSPIRE].

[63] K. Hinterbichler, A. Joyce and R.A. Rosen, *Massive Spin-2 Scattering and Asymptotic Superluminality*, *JHEP* **03** (2018) 051 [arXiv:1708.05716] [INSPIRE].

JHEP06(2024)146

[64] M. Accettulli Huber, A. Brandhuber, S. De Angelis and G. Travaglini, *Eikonal phase matrix, deflection angle and time delay in effective field theories of gravity*, *Phys. Rev. D* **102** (2020) 046014 [arXiv:2006.02375] [INSPIRE].

[65] B. Bellazzini, G. Isabella, M. Lewandowski and F. Sgarlata, *Gravitational causality and the self-stress of photons*, *JHEP* **05** (2022) 154 [arXiv:2108.05896] [INSPIRE].

[66] F. Serra, J. Serra, E. Trincherini and L.G. Trombetta, *Causality constraints on black holes beyond GR*, *JHEP* **08** (2022) 157 [arXiv:2205.08551] [INSPIRE].

[67] C.Y.-R. Chen, C. de Rham, A. Margalit and A.J. Tolley, *A cautionary case of casual causality*, *JHEP* **03** (2022) 025 [arXiv:2112.05031] [INSPIRE].

[68] C. de Rham, A.J. Tolley and J. Zhang, *Causality Constraints on Gravitational Effective Field Theories*, *Phys. Rev. Lett.* **128** (2022) 131102 [arXiv:2112.05054] [INSPIRE].

[69] M. Carrillo González, C. de Rham, V. Pozsgay and A.J. Tolley, *Causal effective field theories*, *Phys. Rev. D* **106** (2022) 105018 [arXiv:2207.03491] [INSPIRE].

[70] S.J. Wallace, *Eikonal expansion*, *Annals Phys.* **78** (1973) 190 [INSPIRE].

[71] S.J. Wallace, *High-energy expansions of scattering amplitudes*, *Phys. Rev. D* **8** (1973) 1846 [INSPIRE].

[72] T.J. Hollowood and G.M. Shore, *Causality Violation, Gravitational Shockwaves and UV Completion*, *JHEP* **03** (2016) 129 [arXiv:1512.04952] [INSPIRE].

[73] E.P. Wigner, *Lower Limit for the Energy Derivative of the Scattering Phase Shift*, *Phys. Rev.* **98** (1955) 145 [INSPIRE].

[74] C. de Rham and A.J. Tolley, *Causality in curved spacetimes: The speed of light and gravity*, *Phys. Rev. D* **102** (2020) 084048 [arXiv:2007.01847] [INSPIRE].

[75] J. Henriksson, B. McPeak, F. Russo and A. Vichi, *Rigorous bounds on light-by-light scattering*, *JHEP* **06** (2022) 158 [arXiv:2107.13009] [INSPIRE].

[76] J. Henriksson, B. McPeak, F. Russo and A. Vichi, *Bounding violations of the weak gravity conjecture*, *JHEP* **08** (2022) 184 [arXiv:2203.08164] [INSPIRE].

[77] K. Häring et al., *Bounds on photon scattering*, arXiv:2211.05795 [INSPIRE].

[78] H. Euler, *On the scattering of light by light according to Dirac's theory*, *Annalen Phys.* **26** (1936) 398 [INSPIRE].

[79] H. Euler and B. Kockel, *The scattering of light by light in Dirac's theory*, *Naturwiss.* **23** (1935) 246 [INSPIRE].

[80] V. Costantini, B. De Tollis and G. Pistoni, *Nonlinear effects in quantum electrodynamics*, *Nuovo Cim. A* **2** (1971) 733 [INSPIRE].

[81] R. Karplus and M. Neuman, *The scattering of light by light*, *Phys. Rev.* **83** (1951) 776 [INSPIRE].

[82] V. Weisskopf, *The electrodynamics of the vacuum based on the quantum theory of the electron*, *Kong. Dan. Vid. Sel. Mat. Fys. Med.* **14N6** (1936) 1 [INSPIRE].

[83] M.-Z. Yang and X.-J. Zhou, *Photon-photon scattering via W boson loops and charged scalar meson loops*, BIHEP-TH-94-13 (1994) [INSPIRE].

[84] V.S. Vanyashin and M.V. Terentev, *The Vacuum Polarization of a Charged Vector Field*, *Zh. Eksp. Teor. Fiz.* **48** (1965) 565 [INSPIRE].

JHEP06(2024)146

[85] H. Epstein, V. Glaser and A. Martin, *Polynomial behaviour of scattering amplitudes at fixed momentum transfer in theories with local observables*, *Commun. Math. Phys.* **13** (1969) 257 [INSPIRE].

[86] M. Froissart, *Asymptotic behavior and subtractions in the Mandelstam representation*, *Phys. Rev.* **123** (1961) 1053 [INSPIRE].

[87] A. Martin, *Extension of the axiomatic analyticity domain of scattering amplitudes by unitarity. 1*, *Nuovo Cim. A* **42** (1965) 930 [INSPIRE].

[88] Y.S. Jin and A. Martin, *Connection Between the Asymptotic Behavior and the Sign of the Discontinuity in One-Dimensional Dispersion Relations*, *Phys. Rev.* **135** (1964) B1369 [INSPIRE].

[89] B. Bellazzini, C. Cheung and G.N. Remmen, *Quantum Gravity Constraints from Unitarity and Analyticity*, *Phys. Rev. D* **93** (2016) 064076 [arXiv:1509.00851] [INSPIRE].

[90] C. de Rham, S. Melville, A.J. Tolley and S.-Y. Zhou, *Massive Galileon Positivity Bounds*, *JHEP* **09** (2017) 072 [arXiv:1702.08577] [INSPIRE].

[91] C. de Rham, S. Melville, A.J. Tolley and S.-Y. Zhou, *Positivity Bounds for Massive Spin-1 and Spin-2 Fields*, *JHEP* **03** (2019) 182 [arXiv:1804.10624] [INSPIRE].

[92] B. Bellazzini, M. Riembau and F. Riva, *IR side of positivity bounds*, *Phys. Rev. D* **106** (2022) 105008 [arXiv:2112.12561] [INSPIRE].

[93] G.F. Giudice, C. Grojean, A. Pomarol and R. Rattazzi, *The Strongly-Interacting Light Higgs*, *JHEP* **06** (2007) 045 [hep-ph/0703164] [INSPIRE].

[94] D. Liu, A. Pomarol, R. Rattazzi and F. Riva, *Patterns of Strong Coupling for LHC Searches*, *JHEP* **11** (2016) 141 [arXiv:1603.03064] [INSPIRE].

[95] C.P. Burgess, *Quantum gravity in everyday life: General relativity as an effective field theory*, *Living Rev. Rel.* **7** (2004) 5 [gr-qc/0311082] [INSPIRE].

[96] C. de Rham and R.H. Ribeiro, *Riding on irrelevant operators*, *JCAP* **11** (2014) 016 [arXiv:1405.5213] [INSPIRE].

[97] R.E. Langer, *On the Connection Formulas and the Solutions of the Wave Equation*, *Phys. Rev.* **51** (1937) 669 [INSPIRE].

[98] A.A. Tseytlin, *Vector Field Effective Action in the Open Superstring Theory*, *Nucl. Phys. B* **276** (1986) 391 [*Erratum ibid.* **291** (1987) 876] [INSPIRE].

JHEP06(2024)146